Shape-shifting structured lattices via multimaterial 4D printing

J. William Boley[a,b,c,1], Wim M. van Rees[b,d,1], Charles Lissandrello[e], Mark N. Horenstein[f], Ryan L. Truby[b,c], Arda Kotikian[b,c], Jennifer A. Lewis[b,c,2], and L. Mahadevan[b,g,h,i,2]

[a]Department of Mechanical Engineering, Boston University, Boston, MA 02215; [b]Paulson School of Engineering and Applied Sciences, Harvard University, Cambridge, MA 02138; [c]Wyss Institute for Biologically Inspired Engineering, Harvard University, Cambridge, MA 02138; [d]Department of Mechanical Engineering, Massachusetts Institute of Technology, Cambridge, MA 02139; [e]Biological Microsystems, Charles Stark Draper Laboratory, Cambridge, MA 02139; [f]Department of Electrical and Computer Engineering, Boston University, Boston, MA 02215; [g]Department of Physics, Harvard University, Cambridge, MA 02138; [h]Department of Organismic and Evolutionary Biology, Harvard University, Cambridge, MA 02138; and [i]Kavli Institute for Nano-bio Science and Technology, Harvard University, Cambridge, MA 02138

Edited by John A. Rogers, Northwestern University, Evanston, IL, and approved September 3, 2019 (received for review May 27, 2019)

Shape-morphing structured materials have the ability to transform a range of applications. However, their design and fabrication remain challenging due to the difficulty of controlling the underlying metric tensor in space and time. Here, we exploit a combination of multiple materials, geometry, and 4-dimensional (4D) printing to create structured heterogeneous lattices that overcome this problem. Our printable inks are composed of elastomeric matrices with tunable cross-link density and anisotropic filler that enable precise control of their elastic modulus (E) and coefficient of thermal expansion (α). The inks are printed in the form of lattices with curved bilayer ribs whose geometry is individually programmed to achieve local control over the metric tensor. For independent control of extrinsic curvature, we created multiplexed bilayer ribs composed of 4 materials, which enables us to encode a wide range of 3-dimensional (3D) shape changes in response to temperature. As exemplars, we designed and printed planar lattices that morph into frequency-shifting antennae and a human face, demonstrating functionality and geometric complexity, respectively. Our inverse geometric design and multimaterial 4D printing method can be readily extended to other stimuli-responsive materials and different 2-dimensional (2D) and 3D cell designs to create scalable, reversible, shape-shifting structures with unprecedented complexity.

4D printing | shape shifting | multimaterial

Shape-morphing structured systems are increasingly seen in a range of applications from deployable systems (1, 2) and dynamic optics (3, 4) to soft robotics (5, 6) and frequency-shifting antennae (7), and they have led to numerous advances in their design and fabrication using various 3-dimensional (3D) and 4-dimensional (4D) printing techniques (8, 9). However, to truly unleash the potential of these methods, we need to be able to program arbitrary shapes in 3 dimensions (i.e., control the metric tensor at every point in space and time), thus defining how lengths and angles change everywhere. For thin sheets, with in-plane dimensions that are much larger than the thickness, this is mathematically equivalent to specifying the first and second fundamental forms of the middle surface. These quadratic forms describe the relation between material points in the tangent plane and the embedding of the middle surface in 3 dimensions and thus, control both the intrinsic and extrinsic curvature of the resulting surface (10, 11). From a physical perspective, arbitrary control of the shape of a sheet requires the design of material systems that can expand or contract in response to stimuli, such as temperature, humidity, pH, etc., with the capacity to generate and control large in-plane growth gradients combined with differential growth through the sheet thickness (12, 13). Such systems are difficult to achieve experimentally; hence, most current shape-shifting structures solutions rarely offer independent control of mean and Gaussian curvatures (14, 15). We address this challenge by 4D printing a lattice design composed of multiple materials.

Beginning at the material level, we created printable inks based on a poly(dimethylsiloxane) (PDMS) matrix, an elastomeric thermoset that exhibits a large operating temperature window and a high thermal expansion coefficient (16). Although the inks are printed at room temperature, the broad range of polymerization temperatures for PDMS enables us to cure the resulting structures at much higher temperatures. On cooling to room temperature, these cured matrices achieve maximal contraction, hence transforming into their deployed states. The same base elastomer is used in all inks to facilitate molecular bonding between adjacent ribs and layers. To create inks with reduced thermal expansivity, we fill the elastomer matrix with short glass fibers (20% wt/wt) that preferentially shear align along the print path (Fig. 1 *A*–*C*) (8, 17). To impart rheological properties suitable for direct ink writing (i.e., a shear yield stress, shear thinning response, and plateau storage modulus) (*SI Appendix*, Fig. S1), we add fumed silica (20 to 22% wt/wt) (*SI Appendix*) to these ink formulations. As an added means of tuning their coefficient of thermal expansion

Significance

Thin shape-shifting structures are often limited in their ability to morph into complex and doubly curved shapes. Such transformations require both large in-plane expansion or contraction gradients and control over extrinsic curvature, which are hard to achieve with single materials arranged in simple architectures. We solve this problem by 4-dimensional printing of multiple materials in heterogeneous lattice designs. Our material system provides a platform that achieves in-plane growth and out-of-plane curvature control for 4-material bilayer ribs. The lattice design converts this into large growth gradients, which lead to complex, predictable 3-dimensional (3D) shape changes. We demonstrate this approach with a hemispherical antenna that shifts resonant frequency as it changes shape and a flat lattice that transforms into a 3D human face.

Author contributions: J.W.B., W.M.v.R., J.A.L., and L.M. designed research; J.W.B., W.M.v.R., C.L., M.N.H., R.L.T., and A.K. performed research; J.W.B., W.M.v.R., C.L., M.N.H., R.L.T., A.K., and L.M. contributed new reagents/analytic tools; J.W.B., W.M.v.R., J.A.L., and L.M. analyzed data; and J.W.B., W.M.v.R., J.A.L., and L.M. wrote the paper.

Conflict of interest statement: J.A.L. is a cofounder of Voxel8, Inc., which focuses on 3-dimensional printing of materials.

This article is a PNAS Direct Submission.

Data deposition: STL files for the 3-dimensional surface mesh used as target shape for Gauss' face and the conformal projection of this face to the plane have been deposited at https://github.com/wimvanrees/face_PNAS2019. The numbering of the faces is consistent between the 2 files, which provides the necessary information to reconstruct the mapping between the 2 shapes.

[1]J.W.B. and W.M.v.R. contributed equally to this work.

[2]To whom correspondence may be addressed. Email: jalewis@seas.harvard.edu or lmahadev@g.harvard.edu.

This article contains supporting information online at www.pnas.org/lookup/suppl/doi:10.1073/pnas.1908806116/-/DCSupplemental.

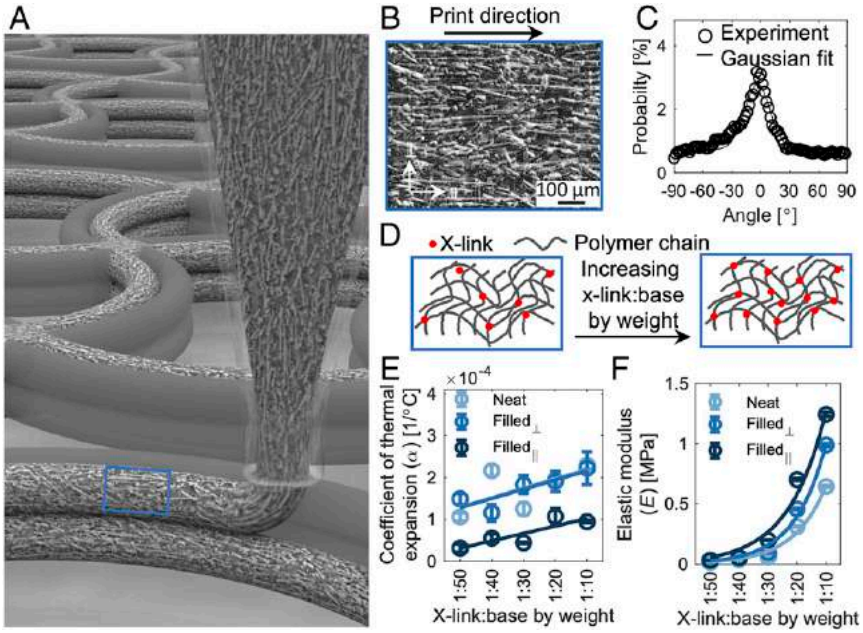

Fig. 1. Printable elastomeric inks with tailored α and E. (*A*) Schematic of a multimaterial 4D printing lattice structure, with ribs depicted as being 2 filaments wide and 2 filaments tall. (*B*) Micrograph of printed fiber-filled filament showing alignment of glass fibers, where $\parallel$ corresponds to the print direction and $\perp$ is perpendicular to the print direction. (*C*) Resulting alignment probability density from *B* showing that the glass fibers align with the print direction, where a 0° angle corresponds to $\parallel$. (*D*) Schematic illustrating varying of x-link to base ratio by weight (x-link:base by weight) for the elastomer matrix. (*E*) Measured α for different ink formulations as a function of x-link:base by weight. Lines represent linear fits to experimental data of the corresponding color. (*F*) Measured E of different ink formulations as a function of x-link:base by weight. Lines represent exponential fits to experimental data of corresponding color.

α and their elastic modulus E, we vary the cross-link to base weight ratio (x-link:base by weight) (Fig. 1*D* and *SI Appendix*) within the elastomeric matrices. Unlike prior work, we generate a palette of 4D printable inks that span a broad range of properties (i.e., α ranges from 32×10^{-6} to 229×10^{-6} 1/°C, while E ranges from 1.5 to 1,245 kPa) (Fig. 1 *E* and *F* and *SI Appendix*, Figs. S2 and S3).

To go beyond the geometric limitation associated with uniform isotropic or anisotropic sheets, we used multimaterial 4D printing to first create simple bilayers (*SI Appendix*, Fig. S4*A*), the basic functional unit of our multiplexed bilayer lattices. The curvature response of these bilayers to a temperature change (ΔT) can be expressed as (18)

$$\frac{\delta\kappa t_2}{\Delta T}=(\alpha_2-\alpha_1)\frac{6\beta\gamma(1+\beta)}{1+4\beta\gamma+6\beta^2\gamma+4\beta^3\gamma+\beta^4\gamma^2}, \qquad [1]$$

where $\delta\kappa=\kappa-\tilde{\kappa}$ is the change in curvature after ΔT, $\tilde{\kappa}$ is the curvature of the bilayer before ΔT, κ is the curvature after ΔT, t is the layer thickness, $\beta=t_1/t_2$, $\gamma=E_1/E_2$, and subscripts 1 and 2 denote the low and high α materials, respectively. The assumptions underlying this equation relate to the nature of the elastic deformation, material characteristics of the rib, and the cross-sectional shape of the layers, and they are further discussed in *SI Appendix*. We use Eq. **1** to delineate a space of dimensionless curvature increments ($\delta\kappa t_2/\Delta T$) with respect to dimensionless bilayer thickness (t_1/t_2) for different ink combinations, which is in good agreement with the corresponding printed bilayers (*SI Appendix*, Fig. S4*B*). The curvature change of our experimental bilayers is reversible and repeatable as demonstrated by thermal cycling experiments (*SI Appendix*, Fig. S4*C*). However, these simple bilayer elements alone do not provide a path to significantly altering the midsurface metric, which is necessary for complex 3D shape changes. For example, the maximum linear in-plane growth that can be achieved with this set of materials, for $\Delta T=\pm250$ °C, is limited to ±6.4%.

To overcome this limitation, we arranged the bilayers into an open cell lattice (19) via multimaterial 4D printing (Fig. 2 *A*–*C*). We consider this lattice a mesoscale approximation of the underlying continuous surface, in which an average metric can now be rescaled with significantly larger growth factors than the largest thermally realizable linear growth of the constituent materials (19, 20). Specifically, if the initial distance between the lattice nodes is denoted $\tilde{L}$ and the initial sweep angle of the ribs is denoted $\tilde{\theta}$, a change in curvature $\delta\kappa$ as computed with Eq. **1** leads to a new distance between lattice nodes L. The linear growth factor, $s=L/\tilde{L}$, of each rib (and hence, of the entire homogeneous isotropic lattice) can be expressed by the following equation:

$$s=\frac{L}{\tilde{L}}=\frac{2\sin\left(\frac{1}{4}\tilde{\theta}\left(2+\frac{\tilde{L}\delta\kappa}{\sin\left(\tilde{\theta}/2\right)}\right)\right)}{2\sin\left(\tilde{\theta}/2\right)+\tilde{L}\delta\kappa} \qquad [2]$$

(*SI Appendix*). In Fig. 2 *B* and *C*, we show 2×2-cell printed lattices of various $\tilde{L}$ and $\tilde{\theta}$, in which ribs undergo a fixed change in curvature ($\delta\kappa\approx72\ \mathrm{mm}^{-1}$ for $\Delta T=250$ °C; computed using Eq. **1**). The measured linear growth for the different $(\tilde{L},\tilde{\theta})$ combinations agrees well with Eq. **2** (Fig. 2*C*) and demonstrates a tremendous range from 79% contraction to 41% expansion. As in the simple bilayer case, these lattices can undergo repeated expansion and contraction in response to a temperature field (Movie S1). Plotting the entire space of growth factors s as a function of $\tilde{\theta}$ (with $-\pi\le\tilde{\theta}\le\pi$) and $\tilde{L}\delta\kappa$ (*SI Appendix*, Fig. S5) reveals that, for $\tilde{L}\delta\kappa\ge2$, it is possible to create ribs that result in $s=0$ (i.e., with arbitrarily large linear contraction ratios). For the considered lattice design, the upper bound for the opening angle is $|\tilde{\theta}|\le|\tilde{\theta}_{\max}|<\pi$, where $\tilde{\theta}_{\max}$ corresponds to the maximum sweeping angle that can be achieved without 2 adjacent ribs touching at their edges so that the minimum value of $\tilde{L}\delta\kappa$ for which $s=0$ will be slightly larger than 2 in reality (*SI Appendix*).

While this homogeneous lattice design can achieve an isotropic rescaling of the Euclidean metric, inducing intrinsic (Gaussian) curvature in an initially planar sheet requires spatial gradients of

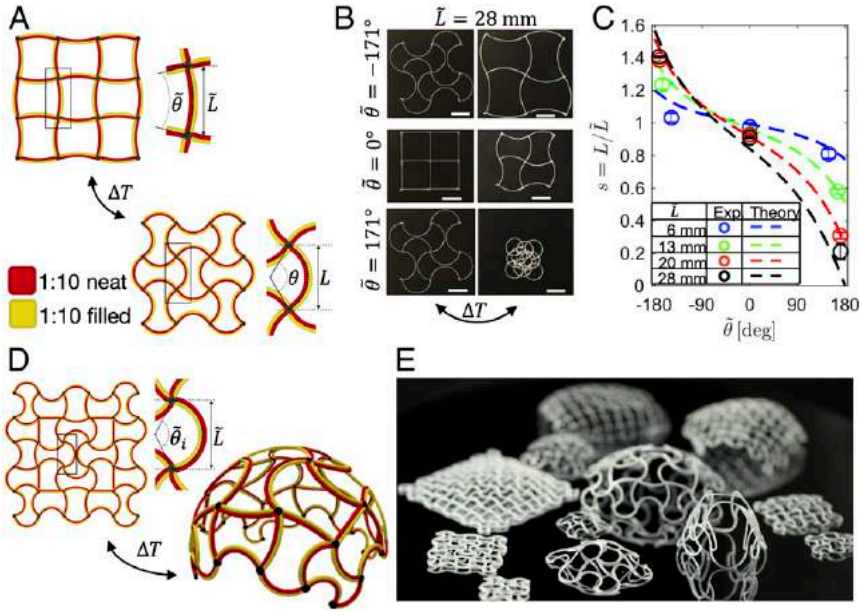

Fig. 2. Multimaterial 4D printing of homogeneous and heterogeneous lattices. (*A*) Schematic of bilayer lattice with defined parameters: printed lattice spacing $(\tilde{L})$ and arc angle $(\tilde{\theta})$ and morphed lattice spacing (L) and arc angle (θ) after applied temperature field (ΔT). (*B*) Images of 2D lattices as printed (*Left*) and after applying a ΔT of −250 °C (*Right*). (Scale bar, 20 mm.) (*C*) Linear growth factor of various printed lattices and their comparison with theory (Eq. **2**) after applying a ΔT of −250 °C. (*D*) Schematic of a 2D heterogeneous lattice design that morphs into a spherical cap under an applied ΔT. (*E*) Photograph of various printed lattices after morphing into spherical caps.

the metric tensor along the surface. To achieve this, we used a heterogeneous lattice in which the initial sweep angle of every rib is considered an independent degree of freedom and is, therefore, indexed within the lattice (Fig. 2*D*). From a conformal map of the desired target shape to the plane, we can compute the required growth factor for each rib and invert Eq. **2** to find the corresponding value of $\tilde{\theta}_i$ (*SI Appendix*). With this approach, we theoretically show the maximum possible opening angle of a grown spherical cap as a function of $\tilde{L}\delta\kappa$ in *SI Appendix*, Fig. S6, demonstrating the theoretical capability of this approach to create a flat lattice that can morph into a complete sphere when $\tilde{L}\delta\kappa \geq 2$ (assuming the idealized case where $\theta_{\max} = \pi$ for simplicity) (*SI Appendix*). We test the efficacy of this approach by transforming flat, square lattices into freestanding spherical caps (Fig. 2 *D* and *E* and *SI Appendix*, Fig. S7) and saddles (*SI Appendix*, Fig. S8). As a preview of multishape possibilities (polymorphism), we leveraged the fact that these PDMS matrices swell when exposed to a variety of solvents (21). We show that a planar lattice programmed to transform into a spherical cap (positive Gaussian curvature) through a negative temperature change can also be transformed beyond its printed configuration to adopt a saddle-shaped geometry (negative Gaussian curvature) when immersed in a solvent (*SI Appendix*, Fig. S9 and Movie S2). Using multimaterial 4D printing, we produced different spherical caps by parametrically varying the number of printed filaments along the width and height of the lattice ribs (N_w and N_h, respectively), the number of cells along either direction of the lattice $(N_x = N_y = N)$, and $\tilde{L}$. One factor affecting these freestanding lattices is their ability to support their own weight without sagging (*SI Appendix*, Fig. S7*A*). At a scaling level, the nondimensional sagging deflection d_s may be written as

$$\frac{d_s}{\tilde{L}} \sim \left(\frac{\bar{\rho}g}{\bar{E}}\right)\left(\frac{\left(N\tilde{L}\right)^3}{h^2}\right), \qquad [3]$$

with $\bar{\rho}$ being the average rib density, g being gravity, h being the rib height, and $\bar{E}$ being the average elastic modulus of a rib (*SI Appendix*). Our experiments confirm that sagging lattices (i.e., when $d_s/\tilde{L}$ is large) also have large values of $\left(\frac{\bar{\rho}g}{\bar{E}}\right)\left(\frac{(N\tilde{L})^3}{h^2}\right)$, but the lattice remains relatively undeformed when $\left(\frac{\bar{\rho}g}{\bar{E}}\right)\left(\frac{(N\tilde{L})^3}{h^2}\right)$ becomes sufficiently small (*SI Appendix*, Fig. S7*A* and Table S1). For the nonsagging structures $(d_s/\tilde{L} < \sim 10)$, the predominant factor affecting their shape transformation is the extent to which the internal α-generated strains can buckle the lattice. We can quantify this by comparing the measured lattice curvature (κ_s) with its theoretical target curvature (κ_t). At a scaling level, the critical strain ϵ_{crit}, above which the lattice is expected to buckle out of plane, is given by (*SI Appendix*)

$$\epsilon_{\text{crit}} \sim \left(\frac{h}{N\tilde{L}}\right)^2. \qquad [4]$$

The experimental lattices that are characterized by large values ϵ_{crit} $(> \sim 6 \times 10^{-4})$ indeed remain flat and do not adopt the curved state (*SI Appendix*, Fig. S7*B*). However, increasing the slenderness of the ribs by either increasing $N\tilde{L}$ or decreasing h reduces the error compared with the theoretical prediction (*SI Appendix*, Fig. S7*B* and Table S1) as expected.

To fully control 3D shape requires the ability to program both the intrinsic curvature and extrinsic curvature. We achieved this by introducing multiplexed pairs of bilayers as ribs within heterogeneous lattices that exploit the large range of α and E values exhibited by our ink palette. Specifically, 4 different materials are used in the cross-sections of each rib, which allows us to control expansion across their thickness and width according to Eq. **1**. We can direct normal curvature up or down by interchanging the top and bottom layers and discretely control its magnitude by transposing the materials in the cross-section as shown in Fig. 3.

Altogether, our multiplexed bilayer rib lattice yields a shape-changing structural framework with 2 significant novelties compared with other motifs. First, these lattices exhibit a substantial amount of local linear in-plane growth (40% growth to 79%

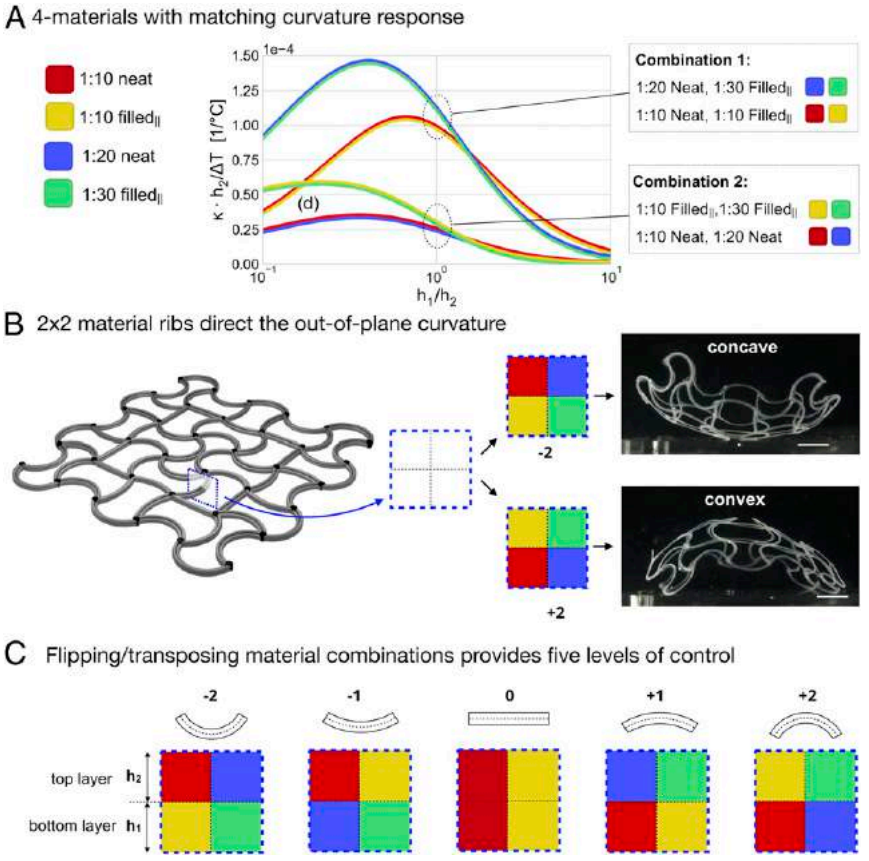

Fig. 3. Multiplex bilayer lattices via multimaterial 4D printing. (*A*) Dimensionless bilayer curvature increments for the 4 different bilayer material combinations. The materials are chosen so that adjacent pairs of equal thicknesses achieve approximately matching curvature increments. While in-plane curvature of each rib is governed by the left–right material pairs and the in-plane opening angle as described in the text and *SI Appendix*, Fig. S5, the out-of-plane curvature of each rib is governed by the top–bottom material pairs according to the graph. (*B*) Schematic of the multiplex bilayer lattice highlighting the cross-section of a rib and 2 experimental examples of 4D printed 4-material hemispherical lattices with maximum concave (*Upper*) and maximum convex (*Lower*) multiplex cross-sections. (Scale bars, 10 mm.) (*C*) Schematics of all possible material combinations for such a cross-section. With 2 materials, the lattice has a symmetric cross-section and 0 mean curvature (labeled 0). Adding 2 more materials enables us to achieve 4 different combinations of out-of-plane curvature ranging from maximum concave (labeled −2) to maximum convex (labeled +2).

contraction as currently demonstrated; 57% times growth to 100% contraction in theory), which can be independently varied across the lattice as well as in each of the 2 orthogonal directions of the lattice. This capability can be generalized to lattices of different scales, materials, and/or stimuli. Second, the out-of-plane bending control reduces elastic frustration, which simplifies their inverse design and expands the range of shapes that can be achieved compared with prior work (8, 22).

To test the capability of our approach to create dynamic functional structures, we innervate these freestanding lattices with liquid metal features composed of a eutectic gallium indium ink that are printed within selected ribs throughout the lattice

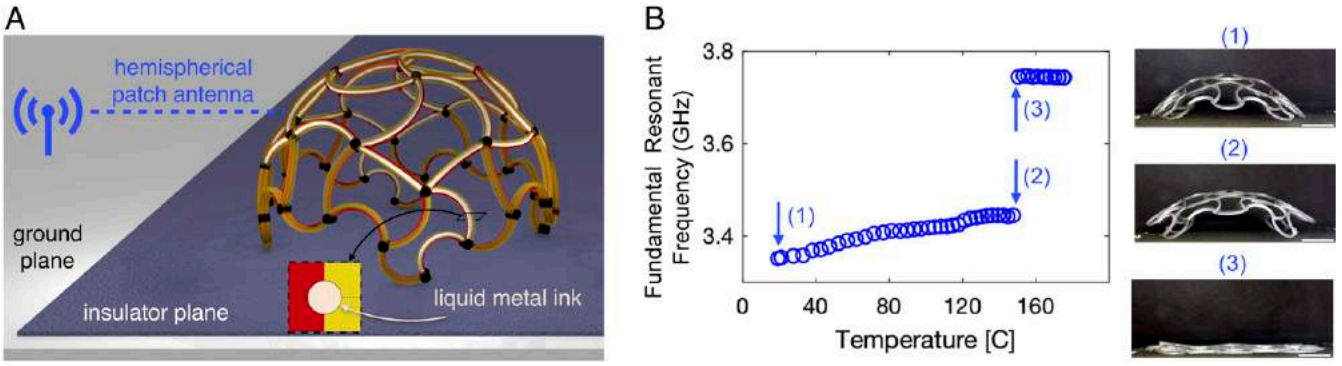

Fig. 4. Shape-shifting patch antenna. (*A*) Schematic of experimental setup for a spherical cap lattice innervated with a liquid metal ink, which is used as a shape-shifting patch antenna. (*B*) Resonant frequency of a printed patch antenna at various temperatures (*Left*) and side view images of the antenna corresponding to different resonant frequencies (*Right*). Parameters for all lattices are as follows: low α material is 1:10 filled$_{\|}$, high α material is 1:10 neat, and $t_1 = t_2 = 0.4$ mm. (Scale bars, 10 mm.)

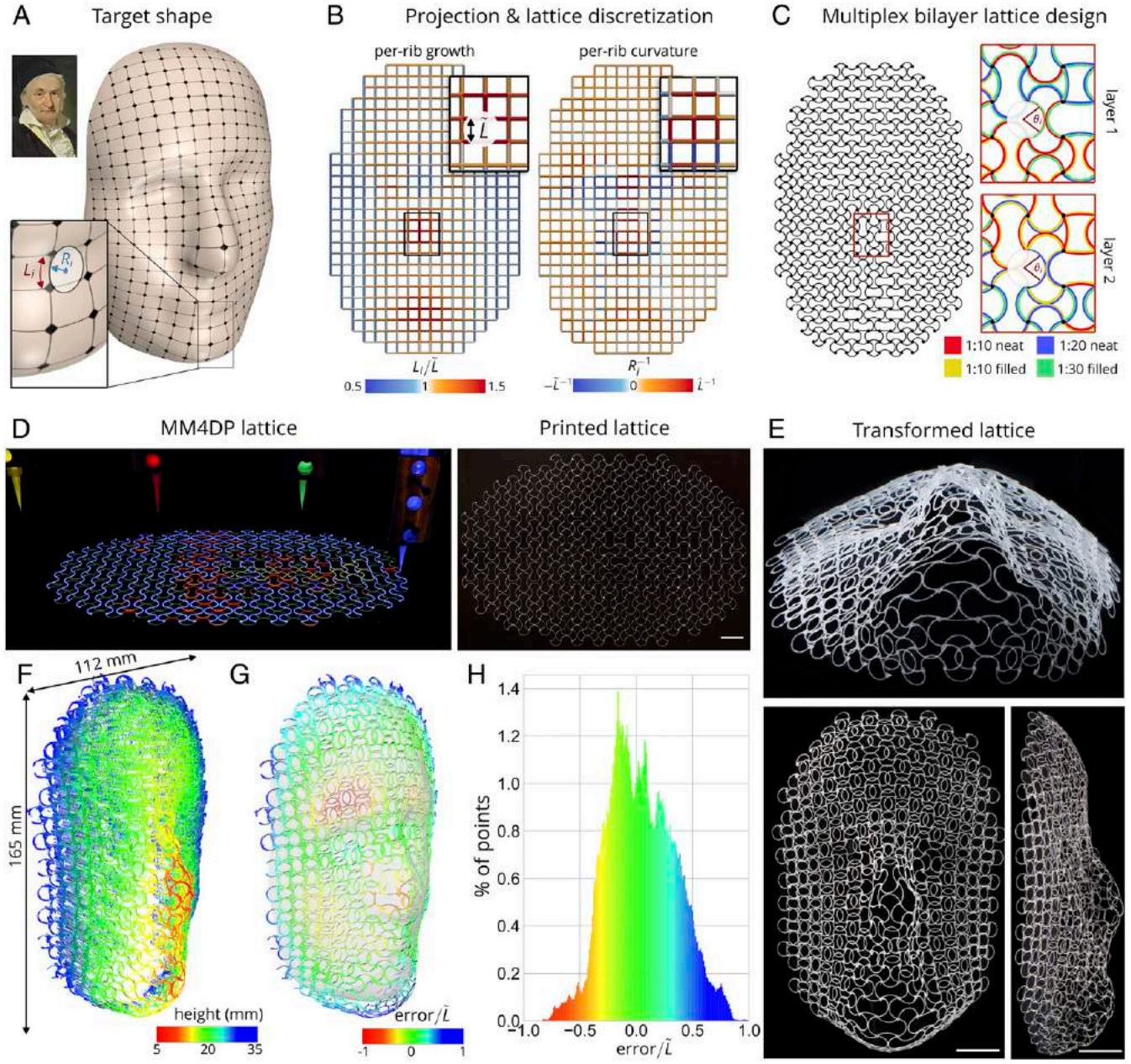

Fig. 5. Integrated design and fabrication of a complex geometrical shape. (*A*) Process for creating a 3D face as the target shape: begin with a 2D image of Carl Friedrich Gauss's likeness (*Upper Left*) and generate a 3D surface (the target shape) via an artificial intelligence algorithm. The detailed view highlights the target length (L_i) and normal radius of curvature (R_i) for 1 specific rib. (*B*) Conformally mapped and discretized lattice with resulting local rib growth $(L_i/\tilde{L})$ and normal curvature (R_i^{-1}), where $\tilde{L} = 10$ mm. (*C*) Programmed multiplex bilayer lattice for printing. Detailed views show a sample area of the programmed lattice, with first and second layers of the lattice showing prescribed $\tilde{\theta}_i$ and multiplex materials. (*D*) Photographs of lattice during (*Left*) and after (*Right*) printing. MM4DP, multimaterial 4D printing. (Note that fluorophores are incorporated in each ink to highlight multimaterial printing.) (Scale bar, 20 mm.) (*E*) Photographs of lattice after transformation. Perspective view (*Upper*), top view (*Lower Left*), and side view (*Lower Right*) of transformed lattice. $\Delta T = -250$ °C. (Scale bars, 20 mm.) (*F*) A 3D scan of the transformed face. (*G*) Normalized error $(\text{error}/\tilde{L})$ of the 3D scan superimposed onto target shape. Negative values represent points that lie below target shape surface. Positive values represent points that lie above target shape surface. (*H*) Distribution of normalized error.

(Fig. 4*A* and *SI Appendix*) to yield a shape-shifting patch electromagnetic antenna (Fig. 4 *A* and *B*). We printed a 2-material lattice $(N_x = N_y = 5, N_w = N_h = 4)$ programmed to change shape into a spherical cap when cooled to room temperature after curing at 250 °C. On reheating this structure, we see a gradual increase in the fundamental resonant frequency as its effective height decreases (Fig. 4*B* and Movie S3). This trend continues until the functional lattice reaches a critical temperature of ∼150 °C, where internal forces can no longer support its weight or provide the appropriate out-of-plane buckling force (i.e., it rapidly returns to its flat-printed geometry). As expected, we observe a sharp increase in the fundamental resonant frequency when this transition occurs. While shape-shifting patch antennae are of interest for wireless sensing and dynamic communication, the ability to integrate conductive ribs could be harnessed for other shape-shifting soft electronic and robotic applications.

To test the capability of our approach to create shapes with complex geometrical features on multiple scales, we printed a planar

lattice that transforms into a human face (Fig. 5 and Movies S4 and S5). We chose to create a simulacrum of the face of C. F. Gauss, father of modern geometry, starting with a 3D target surface mesh (Fig. 5*A*) generated from a painting of Gauss through a machine learning algorithm (23) (*SI Appendix*). We conformally project the face to the plane and discretize the planar projection using a lattice with $\tilde{L} = 10$ mm and $N_x \times N_y = 18 \times 27$ cells truncated to the outline of the surface map. After this discretization, we find among all ribs the maximum and minimum required growth factors $s_{\max} = 1.42$ and $s_{\min} = 0.43$, respectively. The largest growth factors are required near the nose and the chin, where the target mesh has the most substantial Gaussian curvature. We chose ribs with $N_w = N_h = 2$ and generated $\tilde{\theta}_i$ attuned to the required growth by inverting Eq. **2** (*SI Appendix*, Fig. S10). Furthermore, since large parts of the face have almost zero Gaussian curvature, we can rely on our multiplexed bilayer technique to influence the normal curvature independent of the metric transformation (Fig. 5 *B* and *C*). The normal curvature changes sign most prominently near the eye sockets, where the mean curvature undergoes a sign change compared with the rest of the face. With these choices, the lattice dimensionless sagging parameter is $d_s/\tilde{L} \sim \mathcal{O}(10^3)$ (i.e., it cannot support its own weight in air). Immersion of this multimaterial lattice (Fig. 5*D*) in a salt water tank, in which density is only slightly less than the average lattice density (*SI Appendix*), prevents sagging yet allows the lattice to sink to the bottom of the tank (Movie S5). After its shape transformation, the printed lattice shows a clear correspondence to the target geometry (Fig. 5*E*), where the more prominent features of the face, such as the nose, chin, and eye sockets; the finer features associated with the lips and cheeks; and the subtle curvature transitions are all visible. This multiplexed bilayer approach is successful in directing spherical regions up (nose and chin) or down (eye sockets) as required and achieves significant mean curvature near the forehead and around the perimeter of the face, where the Gaussian curvature is small. To test the accuracy of our printed lattice, we obtained a 3D reconstruction of the transformed face (Fig. 5*F*) using a laser-scanning technique (*SI Appendix*). By fitting the scanned data to the target surface (*SI Appendix*), we can compute the smallest distance from each point on the scanned face to the target shape. We use this distance as an error metric and normalize it as error/$\tilde{L}$ (Fig. 5*G*). The distribution of the normalized error (Fig. 5*H*) exhibits a 95% confidence interval within ± 0.62, showing the high accuracy of our multimaterial 4D printing method.

The lattice designs described here are applicable to a wide range of materials, length scales, and stimuli. For example, a lattice with ribs of equal widths ($w_1 = w_2 = w$) and elastic modulus ($E_1 = E_2 = E$) can achieve unbounded contraction when the differential strain between the 2 layers is larger than $8w/3\tilde{L}$. The value of $\tilde{L}$ then determines the range of linear growth that can be achieved, but it also dictates the cell size of the lattice and thereby, the scale of the features that can be captured by the deployed lattice. For a given design, this implies that we should minimize $\tilde{L}$ under the constraint that the required linear growth factors can still be achieved with the specified materials and rib geometry. Independent of $\tilde{L}$ and similar to our theoretical work on bilayer sheets (13), we further expect that there exists a constraint on the maximum target shape curvature that is inversely proportional to the thickness of the ribs.

The lattice architecture can be extended to larger scales of freestanding structures by designing materials with similar α and larger E (and/or smaller ρ) so that, to first approximation, the lattice-based structure would still provide the desired metric changes. Moreover, this approach can be applied to smaller microscale structures by utilizing smaller fillers and nozzle diameters. As these lattice architectures are agnostic to the mode of stimulus, one can imagine designing general lattices with local, variable actuation for myriad materials systems and stimuli [e.g., pneumatics (24, 25), light (26), temperature (27), pH (28), solvent (8, 29), electric field (6), or magnetic field (30)] to transform the same lattice reversibly and dynamically into one or multiple complex shapes.

Our inverse design procedure can be broadened not only to include arbitrary geometries of the underlying lattice but also, to multiplexed bilayers with different material compositions, each of which can be independently varied in space. While we have restricted ourselves to conformal maps and square lattice cells here, our method can be generalized for other projections, spatially varying cell sizes, different tessellations of the plane, and other 2-dimensional (2D) and 3D open cell lattice designs (31–33). By using temperature as stimulus, these lattices can be repeatedly and rapidly (as quickly as ~70ms) (*SI Appendix*, Table S2) actuated in a continuous, well-controlled, and predictable manner. Altogether, our multimaterial 4D printed lattice provides a versatile platform for the integrated design and fabrication of complex shape-morphing architectures for tunable antennae, dynamic optics, soft robotics, and deployable systems that were previously unattainable.

ACKNOWLEDGMENTS. We thank L. K. Sanders and R. Weeks for assistance with manuscript preparation and useful discussions. We acknowledge support from the NSF through Harvard Materials Research Science and Engineering Center Grant DMR-1420570, NSF Designing Materials to Revolutionize and Engineer our Future Grant 15-33985, and Draper Laboratory. W.M.v.R. thanks the Swiss National Science Foundation for support through a postdoctoral grant and the American Bureau of Shipping for support through a Career Development Chair at Massachusetts Institute of Technology. J.A.L. thanks GETTYLAB for their generous support of our work. Any opinions, findings, and conclusions or recommendations expressed in this material are those of the authors and do not necessarily reflect the views of the NSF.

1. K. Saito, S. Nomura, S. Yamamoto, R. Niiyama, Y. Okabe, Investigation of hindwing folding in ladybird beetles by artificial elytron transplantation and microcomputed tomography. *Proc. Natl. Acad. Sci. U.S.A.* **114**, 5624–5628 (2017).
2. M. Mobrem, D. Adams, Lenticular jointed antenna deployment anomaly and resolution onboard the Mars express spacecraft. *J. Spacecr. Rockets* **46**, 403–410 (2009).
3. M. Piovarči, M. Wessely, M. Jagielski Michaland Alexa, W. Matusik, P. Didyk, "Directional screens" in *Proceedings of the 1st Annual ACM Symposium on Computational Fabrication* (Association for Computing Machinery, New York, NY 2017), pp. 1:1–1:10.
4. T. G. Bifano, Microelectromechanical deformable mirrors. *IEEE J. Sel. Top. Quantum Electron.* **5**, 83–89 (1999).
5. M. Wehner *et al.*, An integrated design and fabrication strategy for entirely soft, autonomous robots. *Nature* **536**, 451–455 (2016).
6. E. Acome *et al.*, Hydraulically amplified self-healing electrostatic actuators with muscle-like performance. *Science* **359**, 61–65 (2018).
7. M. Rashed Khan, G. J. Hayes, J. H. So, G. Lazzi, M. D. Dickey, A frequency shifting liquid metal antenna with pressure responsiveness. *Appl. Phys. Lett.* **99**, 013501 (2011).
8. A. S. Gladman, E. A. Matsumoto, R. G. Nuzzo, L. Mahadevan, J. A. Lewis, Biomimetic 4D printing. *Nat. Mater.* **15**, 413–418 (2016).
9. X. Kuang *et al.*, Advances in 4D printing: Materials and applications. *Adv. Funct. Mater.* **29**, 1805290 (2019).
10. K. F. Gauss, *General Investigations of Curved Surfaces* (Princeton University Library, 1902).
11. Y. Klein, E. Efrati, E. Sharon, Shaping of elastic sheets by prescription of non-Euclidean metrics. *Science* 315, 1116–1120 (2007).
12. G. W. Jones, L. Mahadevan, Optimal control of plates using incompatible strains. *Nonlinearity* **28**, 3153–3174 (2015).
13. W. M. van Rees, E. Vouga, L. Mahadevan, Growth patterns for shape-shifting elastic bilayers. *Proc. Natl. Acad. Sci. U.S.A.* **114**, 11597–11602 (2017).
14. S. J. Jeon, A. W. Hauser, R. C. Hayward, Shape-morphing materials from stimuli-responsive hydrogel hybrids. *Acc. Chem. Res.* **50**, 161–169 (2017).
15. H. Ko, A. Javey, Smart actuators and adhesives for reconfigurable matter. *Acc. Chem. Res.* **50**, 691–702 (2017).
16. B. Matthew *et al.*, *Silicones* (Kirk-Othmer Encyclopedia of Chemical Technology, 2002).
17. B. G. Compton, J. A. Lewis, 3D-printing of lightweight cellular composites. *Adv. Mater.* **26**, 5930–5935 (2014).
18. S. Timoshenko, Analysis of bi-metal thermostats. *J. Opt. Soc. Am.* **11**, 233 (1925).
19. R. Lakes, Cellular solid structures with unbounded thermal expansion. *J. Mater. Sci. Lett.* **15**, 475–477 (1996).

20. L. Guiducci *et al*., Honeycomb actuators inspired by the unfolding of ice plant seed capsules. *PLoS One* **11**, e0163506 (2016).
21. J. N. Lee, C. Park, G. M. Whitesides, Solvent compatibility of poly(dimethylsiloxane)-based microfluidic devices. *Anal. Chem.* **75**, 6544–6554 (2003).
22. H. Aharoni, Y. Xia, X. Zhang, R. D. Kamien, S. Yang, Universal inverse design of surfaces with thin nematic elastomer sheets. *Proc. Natl. Acad. Sci. U.S.A.* **115**, 7206–7211 (2018).
23. A. S. Jackson, A. Bulat, V. Argyriou, G. Tzimiropoulos, "Large pose 3D face reconstruction from a single image via direct volumetric CNN regression" in *Proceedings of the IEEE International Conference on Computer Vision and Pattern Recognition* (IEEE, Piscataway, NJ, 2017).
24. R. L. Truby *et al*., Soft somatosensitive actuators via embedded 3D printing. *Adv. Mater.* **30**, e1706383 (2018).
25. J. H. Pikul *et al*., Stretchable surfaces with programmable 3D texture morphing for synthetic camouflaging skins. *Science* **358**, 210–214 (2017).
26. S. J. Park *et al*., Phototactic guidance of a tissue-engineered soft-robotic ray. *Science* **353**, 158–162 (2016).
27. A. Kotikian, R. L. Truby, J. W. Boley, T. J. White, J. A. Lewis, 3D printing of liquid crystal elastomeric actuators with spatially programed nematic order. *Adv. Mater.* **30**, 1706164 (2018).
28. L. D. Zarzar, P. Kim, J. Aizenberg, Bio-inspired design of submerged hydrogel-actuated polymer microstructures operating in response to pH. *Adv. Mater.* **23**, 1442–1446 (2011).
29. J. Kim, J. A. Hanna, M. Byun, C. D. Santangelo, R. C. Hayward, Designing responsive buckled surfaces by halftone gel lithography. *Science* **335**, 1201–1205 (2012).
30. Y. Kim, H. Yuk, R. Zhao, S. A. Chester, X. Zhao, Printing ferromagnetic domains for untethered fast-transforming soft materials. *Nature* **558**, 274–279 (2018).
31. O. Sigmund, S. Torquato, Composites with extremal thermal expansion coefficients. *Appl. Phys. Lett.* **69**, 3203–3205 (1996).
32. R. Lakes, Cellular solids with tunable positive or negative thermal expansion of unbounded magnitude. *Appl. Phys. Lett.* **90**, 221905 (2007).
33. H. Zhu, T. Fan, Q. Peng, D. Zhang, Giant thermal expansion in 2D and 3D cellular materials. *Adv. Mater.* **30**, e1705048 (2018).

Supplementary Information for

Shape-shifting structured lattices via multi-material 4D printing

J. William Boley[*,1,2,3], Wim M. van Rees[*,1,4], Charles Lissandrello[5], Mark N. Horenstein[6], Ryan L. Truby[1,2], Arda Kotikian[1,2], Jennifer A. Lewis[#,1,2], L. Mahadevan[#,1,7]

[1]Paulson School of Engineering and Applied Sciences, Harvard University, Cambridge, MA 02138

[2]Wyss Institute for Bioinspired Engineering, Harvard University, Cambridge, MA 02138

[3]Department of Mechanical Engineering, Boston University, Boston, MA 02215

[4]Department of Mechanical Engineering, Massachusetts Institute of Technology, Cambridge, MA 02139

[5]Charles Stark Draper Laboratory, Cambridge, MA 02139

[6]Department of Electrical and Computer Engineering, Boston, MA 02215

[7]Department of Physics, Department of Organismic and Evolutionary Biology, and Kavli Institute for Nano-bio Science and Technology, Harvard University, Cambridge, MA 02138

Methods

Materials: All elastomeric inks were created by first separately mixing (FlackTek, 120 s at 2000 rpm) the appropriate amount of base and catalyst for two types of PDMS, namely SE 1700 (Dow Corning) with Sylgard 184 (Dow Corning). The neat inks were obtained by combining the resulting pre-mixtures at concentrations of 85% w/w SE 1700 and 15% w/w Sylgard 184, followed by a mixing step (FlackTek, 240 s at 2350 rpm). The filled inks were obtained by combining the SE 1700 and Sylgard 184 pre-mixtures with glass fibers (Fibre Glast, 1/32 inch Glass Fibers, diameter ~ 16 μm, length ~ 230 μm)[1] at concentrations of 68% w/w SE 1700, 12% w/w Sylgard 184, and 20% w/w glass fibers, followed by a mixing step (FlackTek, 240 s at 2350 rpm). Given the presence of fumed silica in SE 1700 (~ 26.5% w/w)[2], the resulting palette of inks contain fumed silica in concentrations ranging from 20% to 22% w/w. As a rheological control, we also created a non-printable mixture (FlackTek, 240 s at 2350 rpm) of 80% w/w Sylgard 184 and 20% w/w of glass fibers. For rheology samples, we replaced the crosslinker with an appropriate concentration of viscosity matched silicone oils (Sigma Aldrich) to avoid any potential crosslinking effects on the rheological measurements. Notably, the printing process lasts less than ~90 minutes, much shorter than the 8-hour pot life of the inks. As such, these crosslinking effects do not occur during the printing process. Inks used to visualize multi-material 4D printing (**Movie M2** and **Fig. 4d**) were dyed with four different fluorophores (Risk Reactor Inc.).

To create functional lattices, we used a liquid metal ink composed of an emulsion of liquid metal (eutectic Gallium Indium (eGaIn), 5N Plus) droplets dispersed into a PDMS (Sylgard567, Dow Corning)

[*]Contributed equally, [#]Corresponding authors, jalewis@seas.harvard.edu, lmahadev@g.harvard.edu

matrix. Specifically, this conductive ink is synthesized by speed-mixing (Flaktek, 4 min at 2350 rpm) a 75% v/v mixture of bulk eGaIn with each of the two parts of PDMS. Next, the two resulting emulsions are mixed together (Flaktek, 4 min at 2350 rpm). The resulting liquid metal ink was then loaded into a 3 cc, Luer-Lok syringes (Nordson, EFD) directly following, centrifuged (300 s at 3500 rpm) to remove bubbles prior to printing.

Ink Rheology: Rheological characterization is carried out using a DHR-3 controlled-stress rheometer (TA Instruments, New Castle, DE, USA) equipped with a 40 mm diameter plate geometry and a gap distance of 1.6 mm. Materials are equilibrated for 30 s at room temperature before flow and amplitude sweep experiments are conducted. In flow sweeps (**Fig. S1a**), the materials are sheared at rates of 0.01 s^{-1} to 10 s^{-1}. Shear storage (G') and loss (G'') moduli (**Fig. S1b**) are measured as a function of shear stress at a frequency of 1Hz during amplitude sweeps. Unlike the control formulation, each ink used in this study exhibits a clear plateau modulus, yield stress, and shear thinning response (**Fig. S1**), which is required for 4D printable formulations due to its fumed silica content. For each of these inks, the plateau modulus (G'_0), yield stress (τ_y), and viscosity (η) exhibit a moderate, yet consistent, decrease with increasing concentration of crosslinker. This is expected, since the crosslinker has a significantly lower viscosity than the base for both SE 1700 and Sylgard 184[2,3]. A modest decrease in G'_0, τ_y, and η is also observed for increasing concentration of glass fibers. This trend is expected[4,5], since the glass fibers (diameter ~ 16 μm, length ~ 230 μm)[1] are significantly larger in size compared to fumed silica particles (~ 7 to 25 nm)[6], effectively resulting in a bimodal mixture.

Multi-Material 4D Printing: For printing experiments, all inks were loaded into separate 10 cc, Luer-Lok syringes (Nordson, EFD) directly following their synthesis. Upon loading, the inks were then centrifuged (300 s at 3500 rpm for neat inks, and 120 s at 2000 rpm for filled inks) to remove bubbles prior to printing. Each syringe was then mounted to one of four independently controlled z-axes of a multi-axis motion system (ABG 1000, Aerotech Inc.), equipped with a tapered nozzle with a 200 μm inner diameter (Nordson, EFD), and connected to an Ultimus V pressure controller (Nordson, EFD). Custom, open source Python libraries (Mecode)[7] were used to define the print paths of each ink during MM4DP and to coordinate printhead motion with ink extrusion. All samples were printed onto Teflon substrates. Typical pressures and print speeds used were 60 psi and 20 mm/s for the neat inks and 72 psi and 16 mm/s for the filled inks. For reference, the time it takes to print the lattice for the face is ~1.5 h.

Filler Alignment: To characterize the alignment of short glass fibers, the low α layer of a representative bilayer strip (40 mm long and 15 mm wide, $t_1 = t_2 = 0.4$ mm, 1:20 filled$_{\parallel}$ low α and 1:10 neat high α) was imaged with a Zeiss microscope system (Discovery V20 with an AxioCam ERc 5s camera and a CL 1500 ECO light source) with the longitudinal edge of the bilayer aligned with the horizontal frame of the microscope. The resulting image was then processed in ImageJ, starting with a grayscale conversion, followed by a background removal (level 50) and a vertical FFT filter to remove any frequencies created by the filaments and by glass fiber alignment along its short axis. The processed image is shown in **Fig. 1b**. The alignment distribution (**Fig. 1c**) was then obtained using ImageJ's directionality plugin.

Thermal Expansion and Elastic Modulus Measurements: Samples (50 mm long, 5 mm wide, and 5 mm tall) were printed for characterizing α for each of our inks (**Fig. S2a** and **b**). After printing, each sample was cured in an oven (Thermo Scientific LB305750M) at 50℃ for 48 h, followed by a thermal cycle on a hot plate (IKA RET basic) at 200℃ for ~0.25 h to ensure curing of the adhesive ingredient. Following this procedure, we loaded the samples into an oven (SHEL LAB SVAC2) with a glass viewport for optical observation. The samples were positioned on precleaned glass slides (Thermo Scientific 2950-001), which are placed on a stainless-steel shelf in the oven. A thin layer (~ 20 μm) of mineral oil (Sigma-Aldrich 161403) was applied to the slides to provide lubrication between the surfaces of the samples and the glass. A calibrated stainless-steel ruler (GEI 2029A-15) was placed next to the samples as a size reference. A digital camera (Nikon D5500) with a macro lens (Sigma 105 mm, f/2.8) was set on a tripod and positioned to view the samples from the side. The oven temperature was increased at a rate of ~ 0.5°C/min from room temperature (~20°C) to 160°C. A remote trigger was used to photograph the samples as the temperature was increased. All images contained the sample and the ruler in the same field of view. Image analysis software (ImageJ) was used to measure the end-to-end length of the sample, using the ruler to calibrate each image. The average resolution of all images used for analysis was determined to be 9.88 μm/pixel. The length data was converted to thermal swelling strain, $\epsilon_{\text{thermal}} = L/\tilde{L} - 1$ and plotted versus the change in temperature, $\Delta T = T - T_0$. α for each sample was determined by fitting the data to the linear relationship $\epsilon_{\text{thermal}} = \alpha \Delta T$ via the 'lsqnonlin' function in MATLAB. The raw data from these experiments are given in **Fig S2c**. A summary of the resulting α for each sample is given in **Fig. 1e**, with the error bars representing the 95% confidence interval of the fit.

Tensile test samples (gauge lengths ~9.5 mm, widths ~4.0 mm, and thicknesses ~0.9 mm), were

printed to characterize the elastic modulus for each ink. After printing, each sample was cured in an oven (Thermo Scientific LB305750M) at 50℃ for 48 h, followed by a thermal cycle on a hot plate (IKA RET basic) at 200℃ for ~0.25 h to ensure curing of the adhesive ingredient. Following this procedure, each sample was tested under uniaxial tension in a single-axis mechanical tester (Instron 5566) at an engineering strain rate of $0.026\,\mathrm{s}^{-1}$ for engineering strains from 0 to 1 (**Fig. S3a**). The resulting engineering stress/strain (σ/ϵ) data is represented in **Fig. S3b**. The elastic modulus (E) of each sample was determined by fitting the low strain data ($0 \leq \epsilon \leq 0.4$) to the linear relationship $\sigma = E\epsilon$ via the 'lsqnonlin' function in MATLAB. A summary of the resulting E for each sample is given in **Fig. 1f**, with the error bars representing the 95% confidence interval of the fits. To confirm that the low strain range is maintained in our printed bilayers, we can use the expression for the maximum stress in material i of the bilayer ($\sigma^i_{\max}$) occurring at the bearing surface between materials i and j[8]:

$$\sigma^i_{\max} = \delta\kappa\left(\frac{4E_i{t_i}^3+3E_i{t_i}^2t_j+E_j{t_j}^3}{6t_i(t_i+t_j)}\right) \tag{S1}$$

From this equation, we can find the maximum strain at the bearing surface through:

$$\epsilon_{\max} = \max\left(\frac{\sigma^1_{\max}}{E_1}, \frac{\sigma^2_{\max}}{E_2}\right) \tag{S2}$$

Evaluating this expression over all bilayer combinations of our inks results in a maximum value of $\epsilon_{\max} \approx 0.03 \ll 0.4$, thus confirming our low strain elastic modulus approximation.

Bimetallic Strip: Eq. (1) relies on several assumptions reported in detail in Timoshenko's original paper[8]. Briefly, the standard assumptions of Euler-Bernoulli beam theory apply, so that plane sections originally normal to the axis of the beam remain plane and normal after deformation. Further, the equations assume uniform material properties throughout each layer, perfect bonding between the layers, and coefficients of thermal expansion that do not change as a function of temperature. Lastly, the specific form of Eq. (1) is obtained using an assumption of rectangular cross-section, although the equations can be expressed in terms of arbitrary cross-sectional area moment of inertia[8].

For our 4D printed structures, the Euler-Bernoulli assumptions may need to be relaxed given that their layer-based thickness ratios can reach 5% for some samples. We have no reason to doubt the uniformity of the material properties within each rib layer, given the experimental procedure described above. The layers are bonded on the molecular level, since the same base elastomer is used in all inks. Of course, for high curvature changes, we cannot rule out the appearance of some friction between the layers. As for any temperature-dependency of the coefficients of thermal expansion, Figure S2 shows some non-

linearity in the thermal strain as a function of temperature. However, our CTE values are determined by a fitting process of this experimental data across a large temperature range (see above and **Fig. S2**), so we expect this effect to be masked by the fit. Lastly, the cross-sectional shape of our layers likely deviates from the assumed square shape. While the nozzle has a circular cross-section, the viscoelastic nature of the material and the effects of gravity the layers induce a non-circular, possibly top-bottom asymmetric, shape. We chose to not take this into account, since this would at most change the prefactor in the second moment of area, e.g. from $\frac{1}{12} \approx 0.08$ for a rectangular cross-section to $\frac{\pi}{64} \approx 0.05$ for an elliptical shape within the same bounding box. Lastly, we note on this topic that the experimental results and theoretical predictions based on Equation (1) (**Fig S4** here, and **Fig 2c** in the main text) agree sufficiently well for us to continue with this form of the equation.

Bilayer Curvature Characterization: Simple bilayer constructs of various material combinations and thicknesses were printed for comparison with Timoshenko theory and to test thermal cycling. These samples each had printed widths and lengths of $\sim$12 mm and $\sim$40 mm, respectively. After printing, each sample was cured in an oven (Thermo Scientific LB305750M) at 50℃ for 48 h, followed by a thermal cycle on a hot plate (IKA RET basic) at 200℃ for ~0.25 h to ensure curing of the adhesive ingredient. Following this procedure, for the data shown in **Fig. 2b**, each sample was loaded into an oven equipped with a viewing window (Across International, AccuTemp-09w), which was then set to a prescribed temperature that was monitored with a k-type thermocouple connected to a digital multimeter (Fluke 179). Upon reaching an equilibrium temperature for 0.5 h, a side view calibrated image of the curved bilayer was captured (Canon EOS 5D Mark III). The curvature of each sample was then extracted from each image using a custom MATLAB script that fits a circle to the side view of the bilayer via 'lsqnonlin'. A summary of the resulting data is shown in **Fig. 2b**, with the error bars representing the 95% confidence interval of the fits. The thermal cycling data shown in **Fig. 2c** was obtained by loading a cured bilayer sample (1:10 filled$_{\|}$ low α ink, 1:10 neat high α ink, $t_1 \sim 0.08$ mm, $t_2 \sim 0.35$ mm) into a thermal cycling unit equipped with a viewing window (TPS, TUJR-A-WF4). The temperature of the unit was then cycled between 20℃ and 130℃ with a heating and cooling rate of 5 ℃/min. with a dwell of 1.33 h to ensure thermal equilibrium. Calibrated sideview images of the bilayer were captured (Canon EOS 5D Mark III) throughout the cycling experiment at 77 s intervals. The curvature of each sample was then extracted from each image using a custom MATLAB script that fits a circle to the side view of the bilayer via 'lsqnonlin'. A summary of the curvature extracted at 130℃ for each cycle is shown in **Fig. 2c**.

Linear Growth Characterization of Homogeneous Lattices: Homogeneous lattices of varying $\tilde{L}$ and $\tilde{\theta}$ were printed to test growth capabilities and compare with theory. These 2×2-cell printed lattices had a fixed low α ink (1:10 filled$_{\|}$), high α ink (1:10 neat), and number of filaments along the rib width and height ($N_w = N_h = 4$). Prior to curing, the configuration of the as-printed lattices captured using a calibrated image (Canon EOS 5D Mark III). Following as-printed imaging, samples were cured in an oven (Thermo Scientific, Hermatherm 0MH100-S) at 275℃ for 0.75 h. After curing, the samples were removed from the oven and transferred to a room temperature substrate where they were allowed to cool and consequently change shape. The transformed configuration of the lattices was captured using the same procedure as the as-printed configuration. The pre- and post- transformation images were then analyzed using a custom MATLAB script to compare the relative position of the lattice nodes, thereby extracting s for each lattice that are summarized in **Fig. 2f**. The error bars in **Fig. 2f** represent the standard deviation of s for the 12 ribs of a given lattice.

Curvature Characterization of Spherical Cap Lattices: Heterogeneous square ($N_x = N_y = N$) lattices of various $\tilde{L}$, N, N_w, and N_h were printed to change shape into prescribed (see *Details of Spherical Cap Lattice Design*) spherical cap geometries. These printed lattices had a fixed low α ink (1:10 filled$_{\|}$) and high α ink (1:10 neat). Following the printing process, samples were cured in an oven (Thermo Scientific, Hermatherm 0MH100-S) at 275℃ for 0.75 h. After curing, the samples were removed from the oven and transferred to a room temperature substrate where they were allowed to cool and consequently change shape. Following shape transformation, calibrated top and side view images of the transformed spherical caps were then captured (Canon EOS 5D Mark III). A custom MATLAB script was used to extract the 3D position of the lattice nodes for each sample and fit the node locations to a spherical surface using 'lsqnonlin', thereby extracting the spherical curvature for each lattice. The results are summarized in **Fig. S7b** and **Tbl. S1**. The error bars in **Fig. S7b** represent the 95% confidence interval of the fit.

Hemispherical Patch Antennas: A hemispherical patch antenna was realized by innervating a selected number of ribs of a two-material lattice by printing a liquid metal ink. The two materials used for the lattice are identical to those used for the heterogeneous square lattices and the lattice parameters are $N = 5$, $\tilde{L} = 12.9$ mm and $N_w = N_h = 4$. The antenna is produced by printing the first two layers of the lattice followed by printing the liquid metal ink in the center of a subset of the lattice ribs. Next, the liquid metal

features are sealed and the top two layers are printed to complete the lattice. The printed functional lattices are polymerized at a high temperature and cooled to room temperature to transform their shape into a spherical cap geometry. The dispersed liquid metal droplets are coalesced mechanically within the ribs of the lattice by rolling across the structure using a polyvinyl chloride tube.

Electrical connections are made by first creating a pilot hole by puncturing the side the corner nodes with a tin-plated copper wire (diameter of approximately 0.4 mm). Next, a short segment of a thinner (diameter of approximately 0.2 mm) silver wire is fed into the rib until it is fixed to the structure by friction. This procedure is repeated on the opposite corner of the lattice. A resistance measurement (Fluke 179) of 50 Ω across confirmed that the liquid metal wiring is conductive. To facilitate further electrical measurements, a longer headphone wire is soldered to silver wire at one of the corners of the lattice and the other wire is removed. The shape-shifting patch antenna is formed by placing the structure upright onto an aluminum ground plane separated by a thin (approximately 0.1 mm) silicon carbide sheet. The assembly is then placed inside a thermal cycling unit equipped with a viewing window and a breakout port for making electrical connections (TPS, TUJR-A-WF4). The wire connected to the lattice is fed from the thermal cycling unit through the breakout port and connected to a precision LCR meter (Agilent E4980A, with a probe frequency of 2 MHz and a probe voltage of 1V). Another wire is connected to the ground plane and fed through the gasket of the front door of the thermal cycling unit (away from the patch antenna wire to avoid stray capacitance) and connected to the precision LCR meter to complete the circuit. To demonstrate the shape-shifting patch antenna, we heated the thermal cycling unit at a rate of $3.5℃ \cdot \mathrm{min}^{-1}$ and tracked the temperature along with side view images of the structure (Canon EOS 5D Mark III) as well as the capacitance between the hemispherical patch antenna and the ground plane. This data is recorded each minute. After the experiment, we removed the lattice while keeping all electrical connections fixed and recorded a tare capacitance of 14.48 pF, which is subtracted from our measurements to obtain the true capacitance between the hemispherical patch antenna and the ground plane. From the true capacitance, we estimated the fundamental resonant frequency (f_{10}) of the patch antenna through the following equation for a rectangular patch antenna[9]

$$f_{10} = \frac{c}{2L_e\sqrt{\varepsilon_e}}$$

where $\varepsilon_e = 1.0$ is the effective relative permittivity (taken to be 1.0 since the patch antenna is separated primarily by air), $c = 3.0 \times 10^8 \mathrm{m} \cdot \mathrm{s}^{-1}$ is the speed of light, and $L_e = L + 2\Delta L$ is the effective length showing the field fringing at the end of the patch antenna; where

$$\Delta L = 0.412h\frac{0.8}{0.242}\frac{W/h + 0.264}{W/h + 0.813}$$

$L = W = 116.1$ mm; where L and W are the effective length and width of the patch antenna (the liquid metal wiring is innervated throughout the ribs comprising a 3×3 lattice interior to the overall 5×5 lattice, and h, the effective height of the hemispherical patch antenna above the ground plane can be estimated from the equation for a planar, two electrode capacitor:

$$h = \varepsilon_0 \frac{LW}{C}$$

where $\varepsilon_0 = 8.85 \times 10^{-12}\ \mathrm{F \cdot m^{-1}}$ is the permittivity of free space and C is the measured capacitance between the hemispherical patch antenna and the ground plane. The results of f_{10} are presented in **Fig. 2g** of the manuscript.

Shape-shifting kinetics: We consider the time scale required for our lattices to reach their equilibrium shape during thermal cycling. On one hand, the lattice ribs will require a finite amount of time τ_e to expand in response to a given temperature, which can be approximated by[10]:

$$\tau_e \approx \frac{\tilde{L}}{9c_s\alpha\Delta T} \tag{S3}$$

where c_s is the speed of sound in the ribs. Using the conservative value of $c_s \approx 1030\ \mathrm{m \cdot s^{-1}}$, which is for PDMS[11], rather than the significantly higher value for glass ($\sim 4200\ \mathrm{m \cdot s^{-1}}$)[12], and conservative values for our lattice structures ($\tilde{L} = 0.02$ m, $\alpha = 4.4 \times 10^{-5}\ ^{\circ}\mathrm{C}^{-1}$, and $\Delta T = 250^{\circ}\mathrm{C}$), results in $\tau_e \approx 0.2$ ms. On the other hand, their thermal response time is limited by how quickly the thermal energy (i.e., temperature) of the bilayer can be increased or decreased in response to ambient conditions. For this, we consider a bilayer of length, $L = 10$ mm with a rectangular cross-section of width, $W = 0.4$ mm and height, $H = 0.4$ mm. The solution to the dynamic average temperature, $\varphi_{\mathrm{m}}(t)$ of the bilayer can be approximated as[13]:

$$\varphi_{\mathrm{m}}^{+}(t) \approx \frac{\varphi_{\mathrm{m}}(t) - \varphi_s}{\varphi_{\mathrm{m}}(0) - \varphi_s} = \varphi_{\mathrm{mPl}}^{+}\left(\frac{4c\rho t}{\lambda W^2}, \frac{\zeta W}{2\lambda}\right) \cdot \varphi_{\mathrm{mPl}}^{+}\left(\frac{4c\rho t}{\lambda H^2}, \frac{\zeta W}{2\lambda}\right) \cdot \varphi_{\mathrm{mPl}}^{+}\left(\frac{4c\rho t}{\lambda L^2}, \frac{\zeta W}{2\lambda}\right) \tag{S4}$$

where

$$\varphi_{\mathrm{mPl}}^{+}\left(\frac{4c\rho t}{\lambda W^2}, \frac{\zeta W}{2\lambda}\right) \approx De^{-\frac{4\mu^2\zeta t}{W^2}} \tag{S5}$$

is the first order term in the infinite series solution to the dimensionless average temperature for one-dimensional plate (shown in the width direction as an example), D and μ are the respective first order expansion coefficient and eigenvalue of the system, which are dependent on the Biot number, $B_i =$

$\zeta W/2\lambda$, c is the bilayer specific heat capacity, ρ is the bilayer density, ζ is the average heat transfer coefficient between the bilayer and its surroundings (modeled as constant on all faces of the bilayer), λ is the thermal conductivity of the bilayer, $\varphi_{\mathrm{m}}(0)$ is the initial average bilayer temperature, and φ_s is the temperature of the surrounding medium. The values used for the bilayer material parameters are $\rho = 1.18\ \mathrm{g/cm^3}$, $c = 1019\ \mathrm{J \cdot kg^{-1} \cdot K^{-1}}$, and $\zeta = 0.15\ \mathrm{W \cdot m^{-1} \cdot K^{-1}}$. To capture the extreme case of curing at high temperature (275℃) and cooling down to room temperature (25℃), we set $\varphi_{\mathrm{m}}(0) = 275$℃. We estimated the speed of the response, which depends on the ambient temperature set during cooling and the composition of the surrounding medium, both of which can be varied experimentally. Using air as the medium, the structure is cooled to 25℃ either by placing it a room temperature or in a freezer held at -40℃ for a shorter period of time. We can either immerse the lattice in a saline solution or leave it in air. Finally, we can cool the structure through natural or forced convection. Considering this broad parameter space, the resulting thermal response time can be as low as ~70 ms (saline solution at 0℃ under forced convection) or as high as 1,372 s (air at 25℃ under natural convection). We summarize the thermal response times for each scenario considered in **Tbl. S2**.

Linear Growth Derivation. We explain how to characterize the growth factors as described in **Eq. 2** of the main text. The initial, printed state is a rib in the form of a circular arc with opening angle $\tilde{\theta}$ connecting two nodes a distance $\tilde{L}$ apart, as shown in **Fig. 2a**. The curvature of the circular arc can be computed as:

$$\tilde{\kappa} = \frac{2\sin(\tilde{\theta}/2)}{\tilde{L}} \tag{S6}$$

and the arclength is then given by:

$$\mathrm{L_{arc}} = \frac{\tilde{\theta}}{\tilde{\kappa}} = \frac{\tilde{\theta}\,\tilde{L}}{2\sin(\tilde{\theta}/2)} \tag{S7}$$

For completeness, we note that the following limit holds:

$$\lim_{\theta \to 0} \frac{\theta}{\sin(\theta/2)} = 2 \tag{S8}$$

so that $\mathrm{L_{arc}} = \tilde{L}$ when $\tilde{\theta} = 0$, as expected. When the rib undergoes a given change in curvature $\delta\kappa$, the post-transformation curvature is $\kappa = \tilde{\kappa} + \delta\kappa$. To compute the post-transformation distance between the nodes L, we assume that the arclength of the rib remains constant so that $\mathrm{L_{arc}} = \tilde{\theta}/\tilde{\kappa} = \theta/\kappa$ where θ is the opening angle of the rib after the curvature change. We then find an expression for L as:

$$L = \frac{2\sin\left(\frac{\theta}{2}\right)}{\kappa} \tag{S9}$$

Reformulating the above expression in terms of $\tilde{\theta}$, $\tilde{L}$, and $\delta\kappa$ alone then gives rise to **Eq. 2** in the main

text, which expresses the growth factor $s = L/\tilde{L}$ in terms of the initial sweep angle $\tilde{\theta}$ and the non-dimensional rib curvature change $\delta\kappa\ \tilde{L}$. In **Fig. S5**, furthermore, we analyze this equation by plotting the growth factor as a contour plot for the parameter region $0 \leq\ \delta\kappa\ \tilde{L} \leq 4.5$ and $-\pi \leq\ \tilde{\theta} \leq \pi$. Within this region, the maximum possible growth occurs at $\tilde{\theta} =\ -\pi$ and $\tilde{L}\delta\kappa = 2$, when $s =\ \pi/2$. The minimum growth is $s =\ 0$ which is achieved on the parametric curve expressed by:

$$\tilde{L}\delta\kappa = (2\pi - \tilde{\theta})\ \frac{2\sin(\tilde{\theta}/2)}{\tilde{\theta}} \tag{S10}$$

again for $-\pi \leq\ \tilde{\theta} \leq \pi$ and $\delta\kappa > 0$. Within this range of $\tilde{\theta}$, the smallest possible non-dimensional curvature $\tilde{L}\delta\kappa$ that achieves $s =\ 0$ is $\tilde{L}\delta\kappa = 2$, at $\tilde{\theta} = \pi$. This value is significant, because for curvatures $\tilde{L}\delta\kappa \geq 2$ the ratio of maximum possible growth over minimum possible growth, which sets the domain of shapes that can be grown, reaches infinity, implying that any smooth target metric field can be achieved, up to a scaling factor that determines the actual dimensions of the grown object (see also the inverse-design process section).

In reality, however, the ribs have a finite width, and they would overlap if we chose $\tilde{\theta} = \pi$. The actual maximum absolute sweeping angle $\tilde{\theta}_{\max} < \pi$, instead depends on the required minimum edge-to-edge gap size. Based on the geometry of the ribs as circular arcs, it can be shown that

$$\tilde{\theta}_{\max} = 4\ \tan^{-1}\left(1 - \frac{\lambda + w}{\tilde{L}}\right),$$

where λ is the desired edge-to-edge gap size and w is the width of the ribs (so that each rib has half-width $w/2$). In the idealized case, we simplify using $\lambda = w = 0$ to find $\tilde{\theta}_{\max} = \pi$. In our experiments, however, we limit the range of opening angles according to $\tilde{\theta}_{\max}$ defined in this equation, using λ to be approximately equal to w to prevent different ribs from fusing together. Once $\tilde{\theta}_{\max}$ is determined, it can be substituted into relation **S10** to find the corresponding minimum value of $\tilde{L}\delta\kappa$ at which arbitrary shapes can theoretically be achieved.

Spherical Cap Lattice Design. We design the spherical cap lattices as follows. For each test case we first choose the number of filaments across the width (N_w), the lattice spacing ($\tilde{L}$), the bilayer materials, and the number of cells in the square lattice ($N_x = N_y = N$). Each of these parameters results in a fixed value of $\delta\kappa$ as computed with **Eq. 1** of the main text. For the corresponding non-dimensional curvature change $\tilde{L}\delta\kappa$, the growth factor of each rib s, as a function of $\tilde{\theta}$ is given by **Eq. 2** of the main text. To design the lattices, we then first evaluate the required linear growth factor s_i for each rib, and then invert **Eq. 2** to

find the corresponding initial sweeping angle $\tilde{\theta}_i$.

To find the growth factors s_i, we consider a spherical cap projected onto the plane using the stereographic projection. In this case, the analytic form of the isotropic continuous growth field $s(r)$ is:

$$s(r) = 2\frac{R_s}{R_d}\frac{1}{1+(r/R_d)^2} \tag{S11}$$

where R_s is the radius of the resulting spherical cap, and R_d sets the dimensions of the planar map. For each of our lattices, the goal is to find R_s and R_d to fully exploit the expansion and contraction capabilities of the individual ribs. We start by using **Eq. 2**, together with the $-|\theta_{max}| \leq \tilde{\theta} \leq |\theta_{max}|$ range of the possible sweep angles, to compute the maximum and minimum possible growth factors (denoted s_{max} and s_{min} respectively) of any individual rib. We then want to compute R_s and R_d so that these growth factors are applied to the innermost and outermost ribs, respectively. To do so, we note that for any given lattice with cell size $\tilde{L}$ and linear dimension N, the mid-points of the closest ribs to the center are located at $r_{min} = \frac{\tilde{L}}{2}$. Similarly, the mid-points of the farthest ribs from the center are located at $r_{max} = \tilde{L}\sqrt{\left(\frac{N}{2}\right)^2 + \left(\frac{N-1}{2}\right)^2}$. We then solve the equations $s(r_{max}) = s_{max}$ and $s(r_{min}) = s_{min}$ for the unknown dimensions R_s and R_d, which gives us the fully specified analytic growth field $s(r)$ so that the innermost ribs expand with s_{max} and the outermost ribs contract with s_{min}. For the other ribs, we evaluate this growth field at their mid-points to compute the rib growth factors s_i. Finally, we use Newton's method to numerically invert **Eq. 2** in the main text for each rib, to obtain the initial sweep angles $\tilde{\theta}_i$. The corresponding spherical cap has a theoretical curvature of $\kappa_t = R_s^{-1}$.

We show the effect of $\tilde{L}\delta\kappa$ on the maximum possible opening angle of the spherical cap using a simplified analysis and visual representation in Figure **S6**. Here we combine equation **2** in the main text with equation **S11** above. Following the explanation above, we set $r_{min} = 0$ for convenience, and consider the growth of a disk of radius r_{max} into a spherical cap. The expression for the opening angle as a function of $\tilde{L}\delta\kappa$ then reduces to

$$\varphi = \pi - \cos^{-1}\left(3 - \frac{8}{2+\tilde{L}\delta\kappa}\right) \tag{S12}$$

which is independent of the radius of the initial disk. This expression is plotted in Figure **S6**, both using the non-dimensional expression $\tilde{L}\delta\kappa$ as well as the dimensional value of $\tilde{L}$ using the characteristic properties of the materials considered here to compute $\delta\kappa$. We observe that for $\tilde{L}\delta\kappa \geq 2$, as explained above and in Figure **S5**, we can theoretically obtain infinite reduction in linear size of a single rib, which would result in a fully closed sphere with $\varphi = \pi$.

Spherical Cap Scaling Analysis

For in-plane loadings of the printed planar lattices, Gibson & Ashby[14] provides an estimate of the scaling of the effective stiffness of the lattice:

$$\frac{E_{eff}}{E} \sim \left(\frac{w}{\tilde{L}}\right)^3,$$

where the third power is obtained by assuming that the primary mode of in-plane deformation is caused by bending of the lattice ribs, where $w = w_f N_w$, with w_f the width of a single filament and N_w the number of filaments across the width of the ribs, in our case.

For the 3D spherical cap, we derive a scaling of the sagging deflection using an energetic analysis of a one-dimensional cantilever beam of length L_B. For a tip deflection d_s, the curvature is proportional to $\kappa_s \sim d_s/L_B^2$, so that the bending energy scales as $U_B \sim E\ I_B\ \kappa_s^2\ L_B \sim E\ h^3 w\ d_s^2/L_B^3$. The work done by the gravitational force, on the other hand, scales as $\rho_B g\ h\ w\ L_B d_S$, with $\rho_B g$ the specific weight of the beam. Equating the two and solving for d_S gives:

$$d_S \sim \left(\frac{\rho_B g}{E}\right)\left(\frac{L_B^4}{h^2}\right) \tag{S13}$$

Substituting the representative lattice length scale $L_B \sim N\tilde{L}$ and dividing each side by L_B leads to the scaling relation mentioned in the main text.

To explain the experimental results of the spherical cap, we use some simple scaling relations that relate the strain generated through thermal expansion, to the buckling of the lattice. For a single beam of length L_B, bending into a curvature κ_B induces an internal bending strain energy $U_B \sim E\ I_B\ \kappa_B^2\ L_B$, where E is the Young's modulus and I_B the second moment of area of the cross-section. This curvature κ_B corresponds to linear order to an in-plane compression of $\delta_B \sim w'(x) L_B \sim \kappa_B^2 L_B^3$, with $w(x)$ the deflection of the beam. The work done by a lateral force P_B is then $W_P = P_B\ \delta_B$. Equating this work with the bending energy then gives:

$$P_B \sim \frac{E\ I_B \kappa_B^2\ L_B}{\kappa_B^2 L_B^3} \sim E\ h\ w \left(\frac{h}{L_B}\right)^2 \tag{S14}$$

where we used that $I_B \sim h^3 w$ with h the thickness and w the width of the beam. In our case, the internal force is generated from the thermal expansion with strain ϵ so that $P_B \sim E\ A\ \epsilon \sim E\ h\ w\ \epsilon$. Plugging this into the above relationship and solve for ϵ gives the critical strain required for buckling of the beam:

$$\epsilon \sim \left(\frac{h}{L_B}\right)^2 \tag{S15}$$

For our lattice the representative length $L_B \sim N\tilde{L}$ leading to the scaling law discussed in the main text.

General Inverse Design: The inverse design process of a general, non-trivial shape starts with a three-dimensional triangle mesh of the target shape's mid-surface. We use a numerical library[15] to conformally project the target shape onto the plane. Since the projected planar outline is arbitrarily oriented, we compute the closest fitted rectangle to the outline and rotate the system so that the largest axis of the rectangle aligns with the x axis of the global coordinate system.

Independently, we choose our lattice materials and number of printed layers per rib, so that we can evaluate the single value $\delta\kappa$ that every rib in the lattice will achieve. We also chose an initial rib length $\tilde{L}$ and number of cells in the x dimension of the lattice, N_x. Given these values we rescale our planar shape projection so that the longest dimension of its rectangular outline is equal to $N_x\tilde{L}$, and construct a lattice that covers the rectangle. We then remove those ribs of the lattice that do not cover at least 50% of the planar projection, and subsequently remove those ribs whose nodes are not connected to at least one other rib. This provides us with the geometric definition of a lattice fitting the target shape's planar projection.

From the projection of the target shape we can compute the analytic required growth and curvature field. In particular, by reparametrizing the surface using the (x, y) coordinates of the plane, the conformal projection provides us with a function $\boldsymbol{m}(x, y)$ that maps any point in the plane to a three-dimensional coordinate vector in space. From $\boldsymbol{m}(x, y)$ we can compute the tangent vectors $\boldsymbol{m}_x(x, y)$ and $\boldsymbol{m}_y(x, y)$ on the target surface, where subscripts denote partial derivatives with respect to the specified parameter. We can also compute the unit normal vector field $\hat{\boldsymbol{n}}(x, y) = (\boldsymbol{m}_x(x, y) \times \boldsymbol{m}_y(x, y))/|\boldsymbol{m}_x(x, y) \times \boldsymbol{m}_y(x, y)|$. These together give rise to the first and second fundamental form of the target surface, $a_T(x, y) = d\boldsymbol{m}^T d\boldsymbol{m}$ and $b_T(x, y) = -d\hat{\boldsymbol{n}}^T d\boldsymbol{m}$. Here d denotes the differential operator so that if a function $f: \mathbb{R}^n \to \mathbb{R}^m$, the differential df is a $m \times n$ matrix where the ith column consists of $\partial f/\partial x_i$. These quadratic forms allow us to characterize the required change in length and curvature of infinitesimal vectors between the planar projection and the three-dimensional shape. In particular, for a parametric vector $d\boldsymbol{u}$ defined at coordinates (x, y), the length change when transformed onto the target surface is:

$$s_u = (d\boldsymbol{u}^T a_T\, d\boldsymbol{u})/(d\boldsymbol{u}^T d\boldsymbol{u}) \tag{S16}$$

and the normal curvature on the target surface in direction $d\boldsymbol{u}$ is:

$$\kappa_u^n = (d\boldsymbol{u}^T b_T\, d\boldsymbol{u})/(d\boldsymbol{u}^T a_T\, d\boldsymbol{u}) \tag{S17}$$

Discrete versions of these quadratic forms on triangle meshes are given and further detailed elsewhere[16,17].

For each rib of our lattice, we then use the Eq. S16 to average the growth field along their lengths, which results in a single scalar average growth factor per rib. We do the same for the normal curvature using Eq. S17 to obtain a single scalar average normal curvature for each rib.

At this point, we have a vector of growth factors, s_i, and a vector of normal curvatures, κ_i^n, defined on a lattice with specified dimensions. We have not, however, chosen the size of the target geometry into which we grow, so that the global size of the target shape is an open degree of freedom. We choose this degree of freedom so that the growth field on our lattice best fits the extent of growth available to the ribs. To do so, we define the required growth ratio of the target geometry as $g_{req} = \max_i s_i \,/\, \min_i s_i$, which is independent of the size of the target shape; any global rescaling of the growth factors would leave g_{req} unaltered. We compare this ratio with the achievable growth ratio, $g_{lattice} = s_{max}/s_{min}$, computed by evaluating **Eq. 2** across the range of allowable sweep angles, after substituting our lattice's value of $\tilde{L}\,\delta\kappa$. If the required growth ratio g_{req} is larger than the achievable growth ratio $g_{lattice}$, the shape can not be grown with the input lattice characteristics and we need to revisit our choice of parameters. In particular, increasing $g_{lattice}$ can be achieved by increasing $\tilde{L}\,\delta\kappa$; note that once its value $\tilde{L}\,\delta\kappa \geq 2$, we have $s_{min} = 0$ so the achievable growth ratio becomes infinity (see main text). This means that for such lattices, any smooth shape can be grown, up to a global scaling factor. In practice, we maximize $\tilde{L}\,\delta\kappa$ by choosing the largest possible lattice side length $\tilde{L}$ given a desired resolution N_x, so that the largest dimension of the lattice $\tilde{L}\,N_x$ stays within the limits posed by the experimental setup (in our case the size of the print bead). Simultaneously, we maximize $\delta\kappa$ by reducing the rib half-width to the minimum filament size for our inks. Once we have a lattice for which $g_{lattice} \leq g_{req}$, we scale the desired target shape size by altering our growth factors with a uniform factor f. This rescaling is necessary to make sure that $\max_i(f s_i) \leq s_{max}$ and $\min_i(f s_i) \geq s_{min}$. If $g_{lattice} = g_{req}$, the choice of f is unique, but for $g_{lattice} < g_{req}$we have a degree of freedom in this scaling factor. Here we set $f = 2/(\max_i s_i + \min_i s_i)$ so that the average growth factor, after rescaling, is equal to 1.

Next, we need to choose the multiplex bilayer design for each rib, given the required in-plane growth as well as normal curvature. We do this by comparing the required normal curvature κ_i^n to the possible out-of-plane curvature values of each multiplex design. However, a complication here is that once we change the multiplex bilayer design to achieve the desired out-of-plane curvature, the in-plane $\delta\kappa$ changes as well, which affects the range of in-plane growth that can be achieved. In this work we

prioritize the in-plane growth and choose only multiplex bilayer designs that can achieve the desired in-plane growth, compromising the out-of-plane curvature if necessary. Finally, we compute $\tilde{\theta}_i$. For each rib we compute the respective value of $\tilde{L}\delta\kappa$ using the assigned multiplex materials, and **Eq. 1** in the main text. We then use Newton's method to numerically invert **Eq. 2** in the main text given the required scaled growth factor fs_i, to obtain the initial sweep angles $\tilde{\theta}_i$.

Generating Gauss's Face. To create the three-dimensional model of Gauss's mask, we start with a photographic reproduction of an 1840 painting by Danish painter Christian Albrecht Jensen, which now is available in the public domain (**Fig. 4a**). We feed this image in the open-source Artificial Intelligence 3D face reconstruction software[18]. This software uses a trained convolutional neural network to generate a three-dimensional model of the face in the corresponding image. We then make some substantial manual alterations to the AI-generated output mesh. Firstly, we extract the face surface from the output shape, and regularize the underlying triangle mesh. Secondly, we manually add a forehead starting from 1/4th of an ellipsoidal surface properly dimensioned to fit the face and attached to the model. Lastly, we manually smooth some individual features to regularize the curvature of the target shape. The resulting three-dimensional surface mesh can be downloaded in STL format from the supplementary information.

Face Reconstruction and Error Analysis: To generate a 3D reconstruction of the transformed face, we first placed the lattice in an aquarium full of salt water ($\sim$240 g/L of NaCl). We then attached a laser scanner (Keyence, LJ-V7080) to an automated gantry (Aerotech Inc.). Through a customized set of commands, we scanned the immersed lattice, along with a calibration disc, and synchronized the position data of the gantry with the laser scanner, resulting in the 3D reconstruction of the transformed face. Following this step, we imported the scanned data into an open source point cloud processing software (CloudCompare). Here we processed and denoised the point cloud by performing a density computation and discarding isolated points. We then imported the target shape mesh in the same software, scaled it to its pre-computed physical size given the lattice dimensions and the global scaling factor, and aligned the bounding boxes of the point cloud with the scaled target mesh. To perform the distance computation, we performed a finer alignment of the point cloud with the target mesh according to the Iterative Closest Point (ICP) algorithm (translation and rotation only). We then computed the closest distance for each point in the point cloud to the target mesh according to the built-in routine of CloudCompare and exported the histogram data of this quantity. We finally loaded the colored point cloud and target mesh in the open

source rendering software Blender to generate the images in the main text.

References

1. FIBRE GLAST, FIBRE GLAST 1/32 inch Milled Glass Fibers product data sheet. *2018*
2. DOW CORNING, DOW CORNING SE 1700 safety data sheet. (2018). Available at: https://consumer.dow.com/en-us/pdp.dowsil™ se 1700.01707116z.html?tab=sds&id=01707116z.
3. DOW CORNING, DOW CORNING Sylgard 184 safety data sheet. (2018). Available at: https://consumer.dow.com/en-us/pdp.sylgard™ 184 silicone elastomer kit.01064291z.html?tab=sds&id=01064291z.
4. Farris, R. J. Prediction of the Viscosity of multimodal suspensions from unimodal viscosity data. *Trans. Soc. Rheol.* (1968). doi:10.1122/1.549109
5. Marti, I., Höfler, O., Fischer, P. & Windhab, E. J. Rheology of concentrated suspensions containing mixtures of spheres and fibres. *Rheol. Acta* (2005). doi:10.1007/s00397-005-0432-9
6. W., F. O. *et al.* Silica. *Ullmann's Encyclopedia of Industrial Chemistry* (2008). doi:doi:10.1002/14356007.a23_583.pub3
7. Minardi, J. https://github.com/jminardi/mecode/.
8. Timoshenko, S. Analysis of bi-metal thermostats. *J. Opt. Soc. Am.* (1925). doi:10.1364/JOSA.11.000233
9. Abbasi Layegh, M., Ghobadi, C. & Nourinia, J. The optimization design of a novel slotted microstrip patch antenna with multi-bands using adaptive network-based fuzzy inference system. *Technologies* (2017). doi:10.3390/technologies5040075
10. Lee, Y. C. Speed of thermal expansion of a long, thin insulating bar and the physical momentum of acoustic phonons. *J. Phys. Condens. Matter* (2008). doi:10.1088/0953-8984/20/05/055202
11. Zell, K., Sperl, J. I., Vogel, M. W., Niessner, R. & Haisch, C. Acoustical properties of selected tissue phantom materials for ultrasound imaging. *Phys. Med. Biol.* (2007). doi:10.1088/0031-9155/52/20/N02
12. Thomas M. Proctor, J. Sound speed measurements in solids: absolute accuracy of an improved transient pulse method. *J. Res. Natl. Bur. Stand. (1934)*. **75C**, 33–40 (1971).
13. Baehr, H. D. & Stephan, K. *Heat and Mass Transfer*. (Springer Berlin Heidelberg, 2011).
14. Gibson, L. J. & Ashby, M. F. *Cellular Solids: Structure and Properties*. *Cambridge Solid State Science Series* (Cambridge University Press, 1997). doi:DOI: 10.1017/CBO9781139878326

15. Mullen, P., Tong, Y., Alliez, P. & Desbrun, M. Spectral conformal parameterization. *Eurographics Symp. Geom. Process.* (2008). doi:10.1111/j.1467-8659.2008.01289.x
16. Weischedel, C., Tuganov, A., Hermansson, T., Linn, J. & Wardetzky, M. Construction of discrete shell models by geometric finite differences. in (Fraunhofer ITWM, 2012).
17. van Rees, W. M., Vouga, E. & Mahadevan, L. Growth patterns for shape-shifting elastic bilayers. *Proc. Natl. Acad. Sci.* (2017). doi:10.1073/pnas.1709025114
18. Jackson, A. S., Bulat, A., Argyriou, V. & Tzimiropoulos, G. Large pose 3D face reconstruction from a single image via direct volumetric CNN regression. in *Proceedings of the IEEE International Conference on Computer Vision* (2017). doi:10.1109/ICCV.2017.117

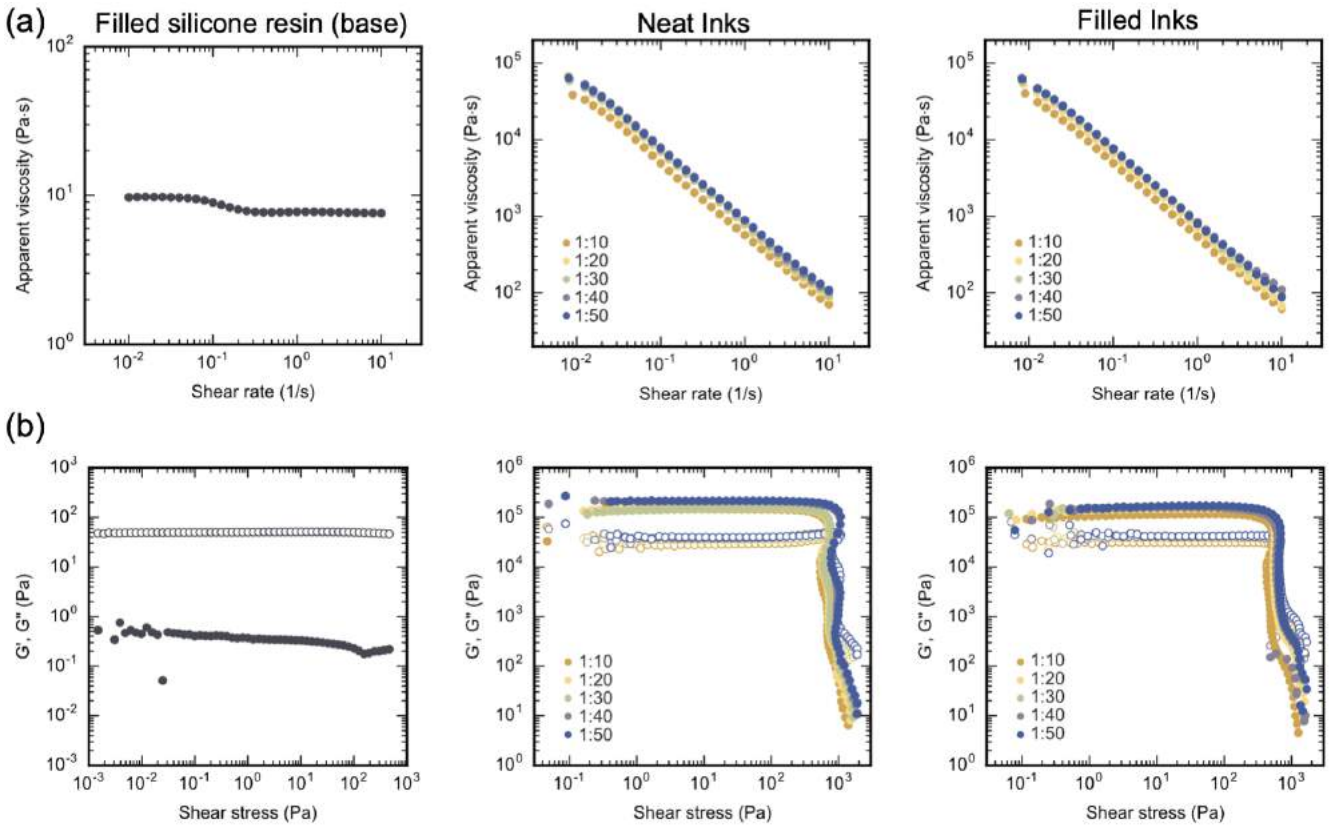

Figure S1. Ink rheology. a) Log-log plots of the apparent viscosity as a function of shear rate for the glass fiber-filled, base silicone resin (left) and the neat (middle) and filled (right) silicone inks. b) Log-log plots of the storage (G', closed circles) and loss (G'', open circles) moduli as a function of shear stress for the filled silicone resin (left) and the neat (middle) and filled (right) silicone inks. All legend labels denote the weight ratios of crosslinking agent to base.

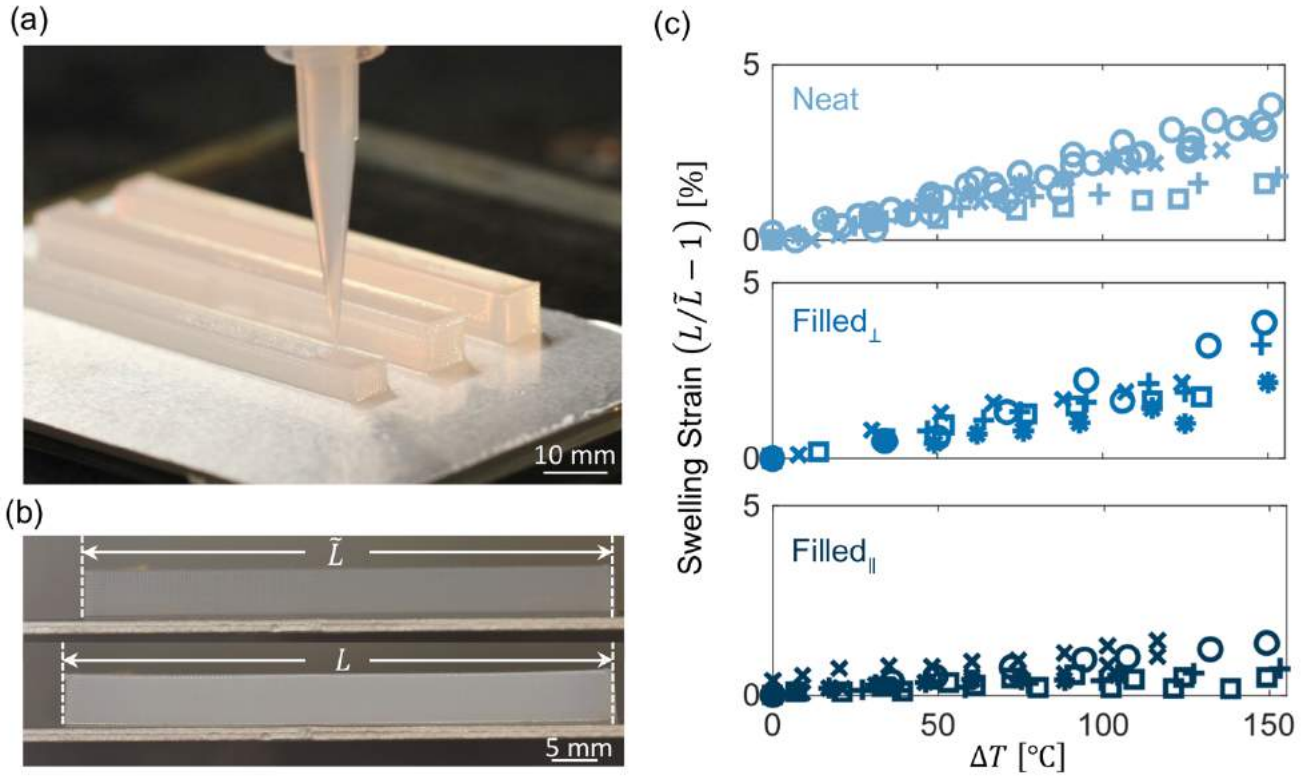

Figure S2. Thermal expansion (α) measurements. a) Image of α test specimens being printed using the 1:10 neat ink. b) Representative image of the as-printed (25℃, top) and expanded (160℃, bottom) states, where the measured lengths are used to calculate α. The ink used to construct these samples is the 1:10 neat. c) Measured swelling strains for neat (top), filled$_\perp$ (middle) and filled$_\parallel$ (bottom) inks. Circles, crosses, stars, and squares represent data for 1:10, 1:20, 1:30, 1:40, and 1:50 weight ratios of crosslinker-to-base silicone inks, respectively.

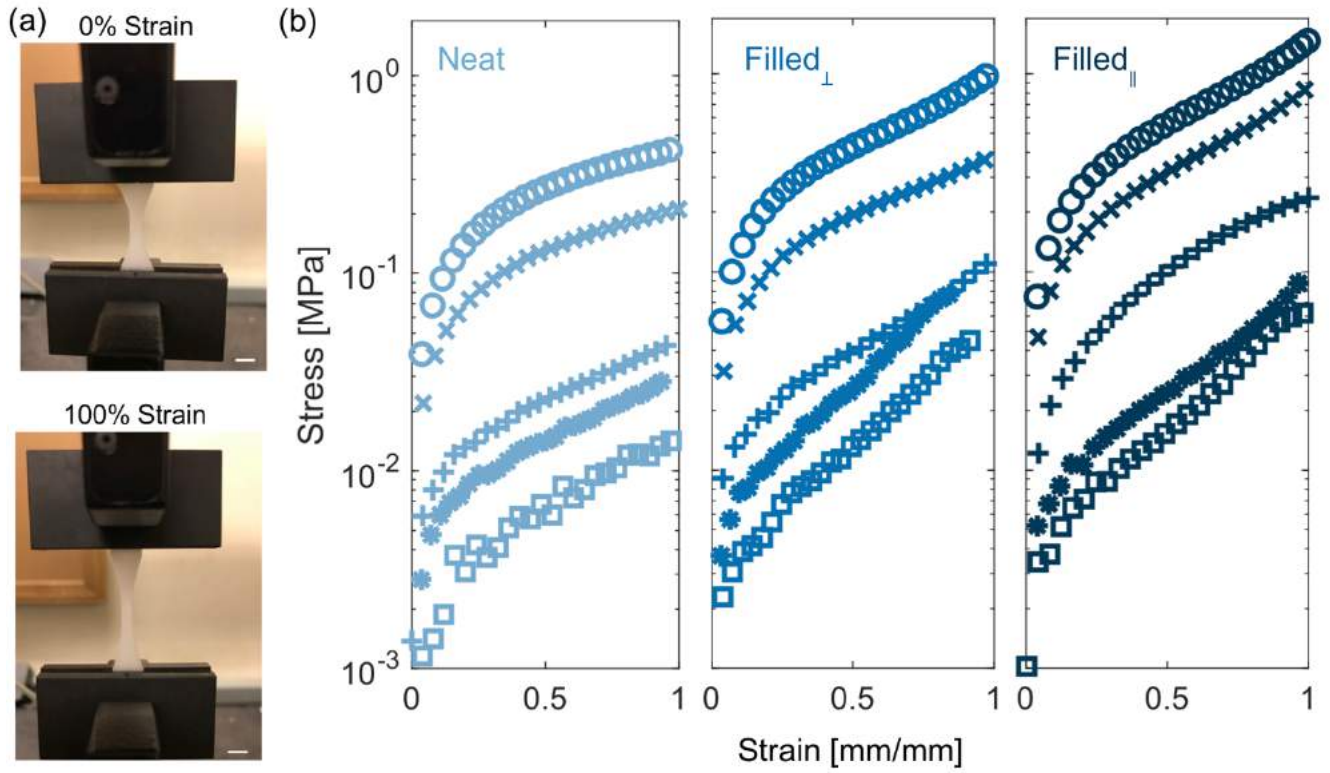

Figure S3. Elastic modulus measurements. a) Images of printed tensile test specimens at 0% (top) and 100% (bottom) strain. Scale bars correspond to 5 mm. The ink used for these specimens is the 1:10 filled$_{\parallel}$. b) Stress versus strain curves of tensile test specimens for neat (left), filled$_{\perp}$ (middle) and filled$_{\parallel}$ (right) inks. Circles, crosses, stars, and squares represent data for 1:10, 1:20, 1:30, 1:40, and 1:50 weight ratios of crosslinker-to-base silicone ink, respectively.

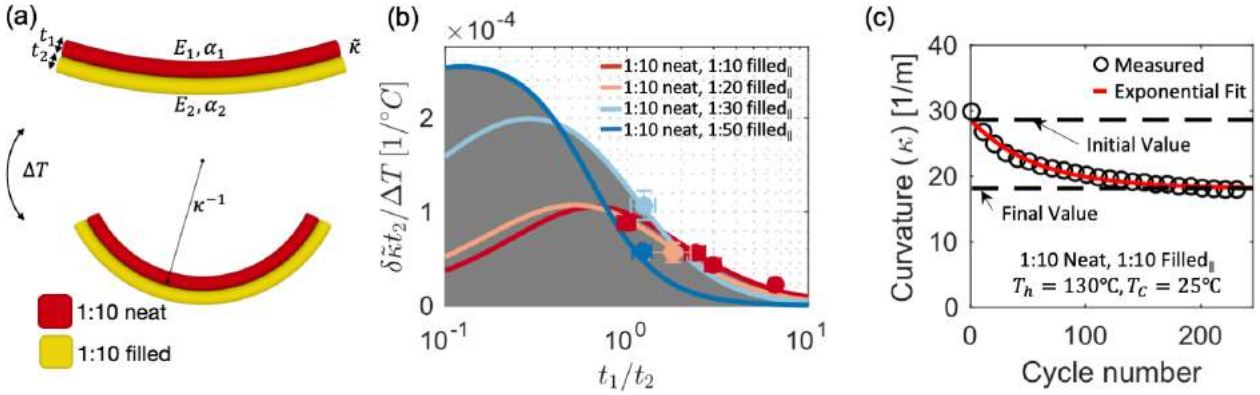

Figure S4. Printed bilayers. a) Schematic of printed bilayer with defined parameters: initial curvature ($\tilde{\kappa}$), layer thicknesses (t_1 and t_2), linear αs (α_1 and α_2), elastic moduli (E_1 and E_2) of the high and low α layers (1 is the low α material and 2 is the high α material), imposed temperature difference (ΔT), and final curvature (κ) under applied temperature difference. b) Phase plot of attainable temperature sensitivity of dimensionless curvature (gray shaded area) with validated experimental data (colored circles). Lines are theoretical predictions (**Eq. 1**). c) Experimental curvature of a thermally cycled bilayer as a function of cycle number.

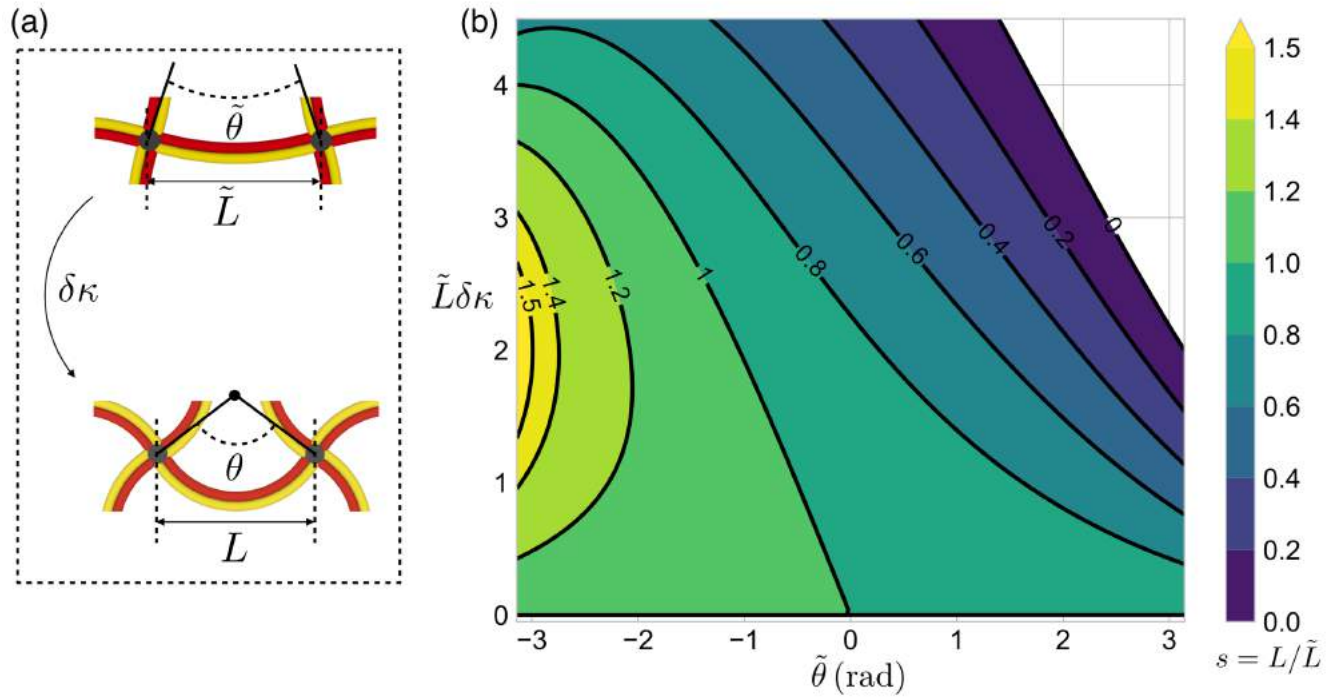

Figure S5. a) A single rib in the lattice is characterized by initial linear length $\tilde{L}$ and opening angle $\tilde{\theta}$ (top), and transforms to a length L and opening angle θ after a curvature change of $\delta\kappa$ (bottom). b) The growth of such a rib quantified in a contour plot, showing the linear growth factor s as a function of the internal opening angle $\tilde{\theta}$ (horizontal axis) and non-dimensional curvature change $\tilde{L}\delta\kappa$ (vertical axis).

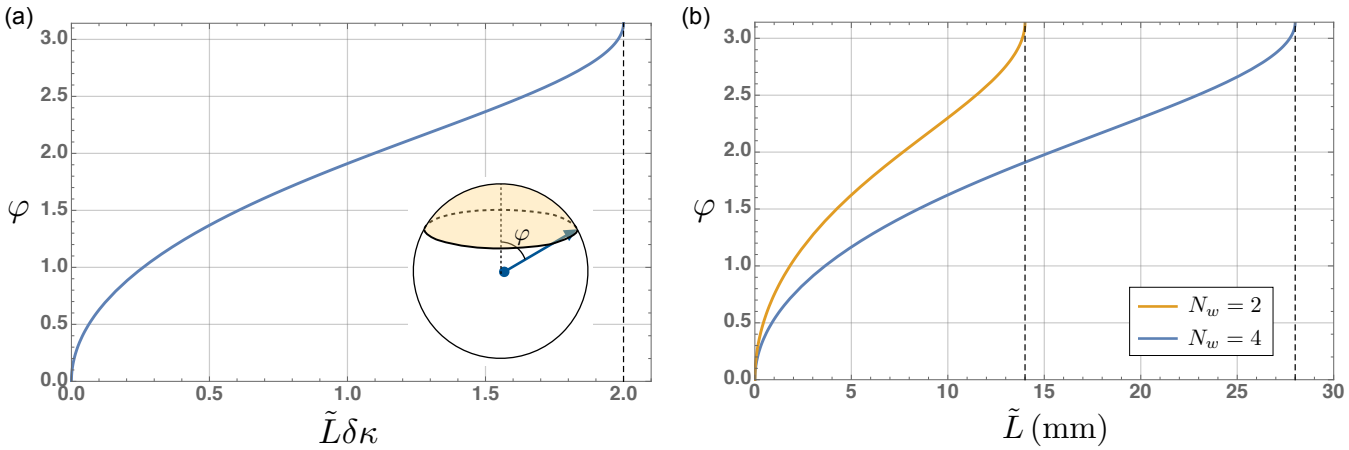

Figure S6. (a) For a planar lattice growing into a spherical cap (using stereographic projection), the graph shows the maximum opening angle φ of the cap as a function of the initial linear length $\tilde{L}$ and maximum curvature change of $\delta\kappa$. The vertical dashed line corresponds to $\tilde{L}\delta\kappa = 2$, above which a rib can theoretically shrink to point as shown in Figure **S5**, resulting in $\varphi = \pi$. (b) The same graph but using a dimensional x-axis corresponding to the material properties of ribs consisting of 1:10 filled$_{\parallel}$ and 1:10 neat materials. Using a cross-section with two filaments in width ($N_w = 2$, orange) enables arbitrary opening angles above $\tilde{L} \approx 14$ mm, when doubling the number of filaments in the cross-section ($N_w = 4$, blue) this critical side length increases to $\tilde{L} \approx 28$ mm.

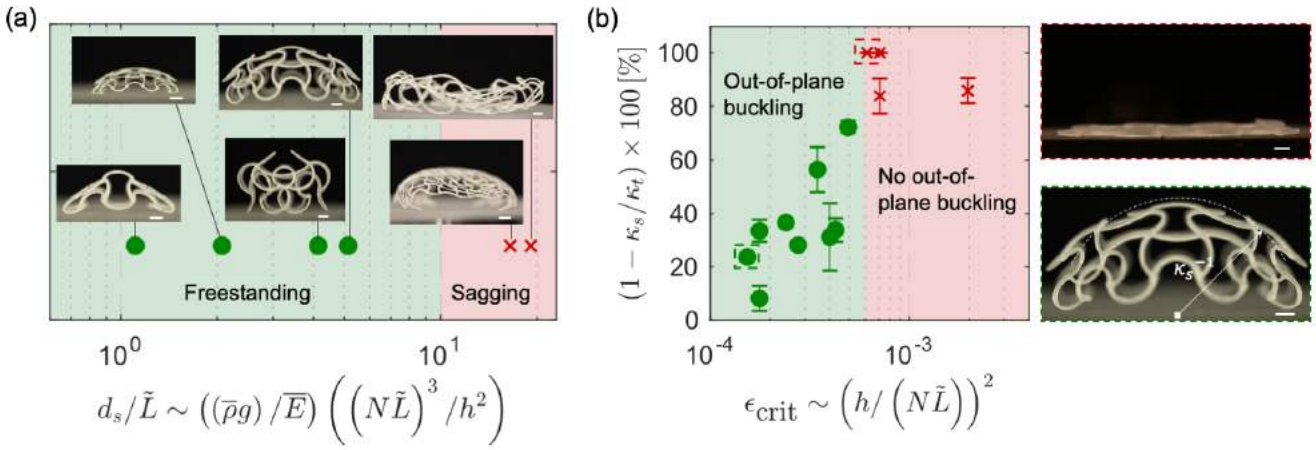

Figure S7. Heterogeneous bilayer lattices can morph into freestanding spherical caps. a) Tradeoff between bending energy and gravitational energy to form freestanding structures in air. Insets are side-view images of various printed hemispherical caps placed onto substrates in air after a ΔT of -250°C. b) (left) Prediction error as a function of internal strain ϵ_{crit} $(\Delta T = -250°C)$. (Top-Right) Representative lattice with a large ϵ_{crit} (6.2×10^{-4}) that does not exhibit out of plane buckling. (Bottom-Right) Representative lattice with small ϵ_{crit} (1.5×10^{-4}) that exhibits out of plane buckling and a low prediction error. The low and high α materials used in these lattices are 1:10 filled$_{\parallel}$ and 1:10 neat, respectively (see **Methods** and **Table S1**).

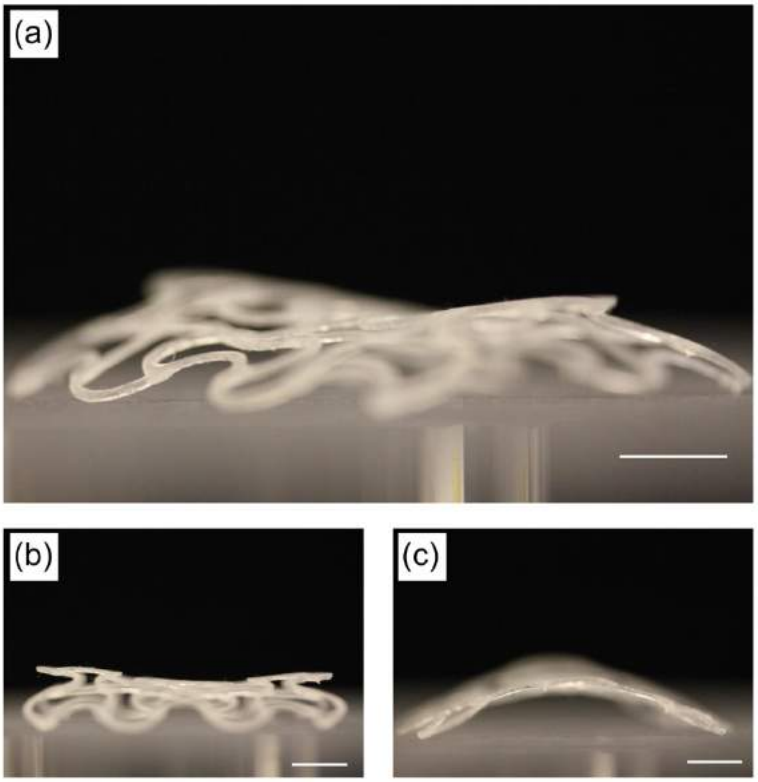

Figure S8. Saddle shaped lattice. Similar to the spherical caps discussed in the main text, imposing a metric corresponding to a negative Gaussian curvature results in a saddle shape of the transformed lattice. The low and high α materials used in these lattices are 1:10 filled$_{\|}$ and 1:10 neat, respectively (see **Methods**), and $\tilde{L} = 6.0$ mm). Scale bars correspond to 5 mm.

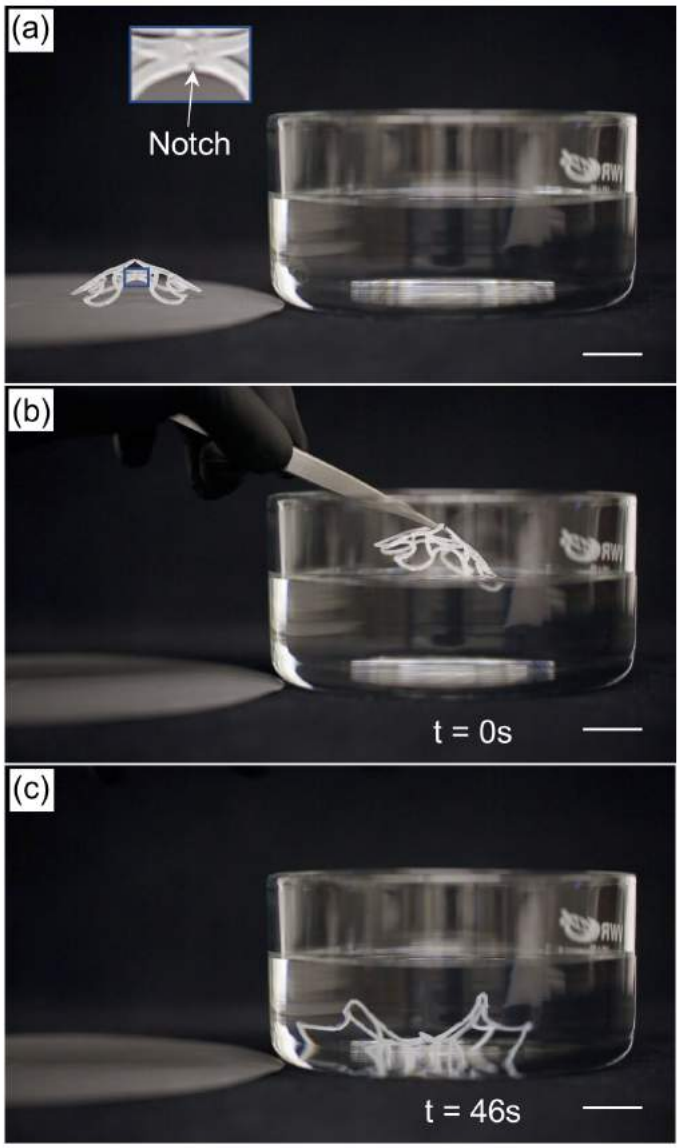

Figure S9. Polymorphing lattice. a) A planar lattice programmed to transform into a spherical cap (positive Gaussian curvature) through a negative temperature change. b) The spherical cap-shaped lattice is immersed into a solvent (i.e., hexane) to induce swelling of the PDMS matrix. c) After 46 sec in hexane, the lattice swells beyond its printed configuration to adopt a saddle shape geometry (negative Gaussian curvature). The low and high α materials used in these lattices are 1:10 filled$_{\parallel}$ and 1:10 neat, respectively, and $\tilde{L} = 12.9$ mm (see **Methods**). We printed the lattice with small notches (shown in a) to help guide the extrinsic curvature. Scale bars correspond to 20 mm.

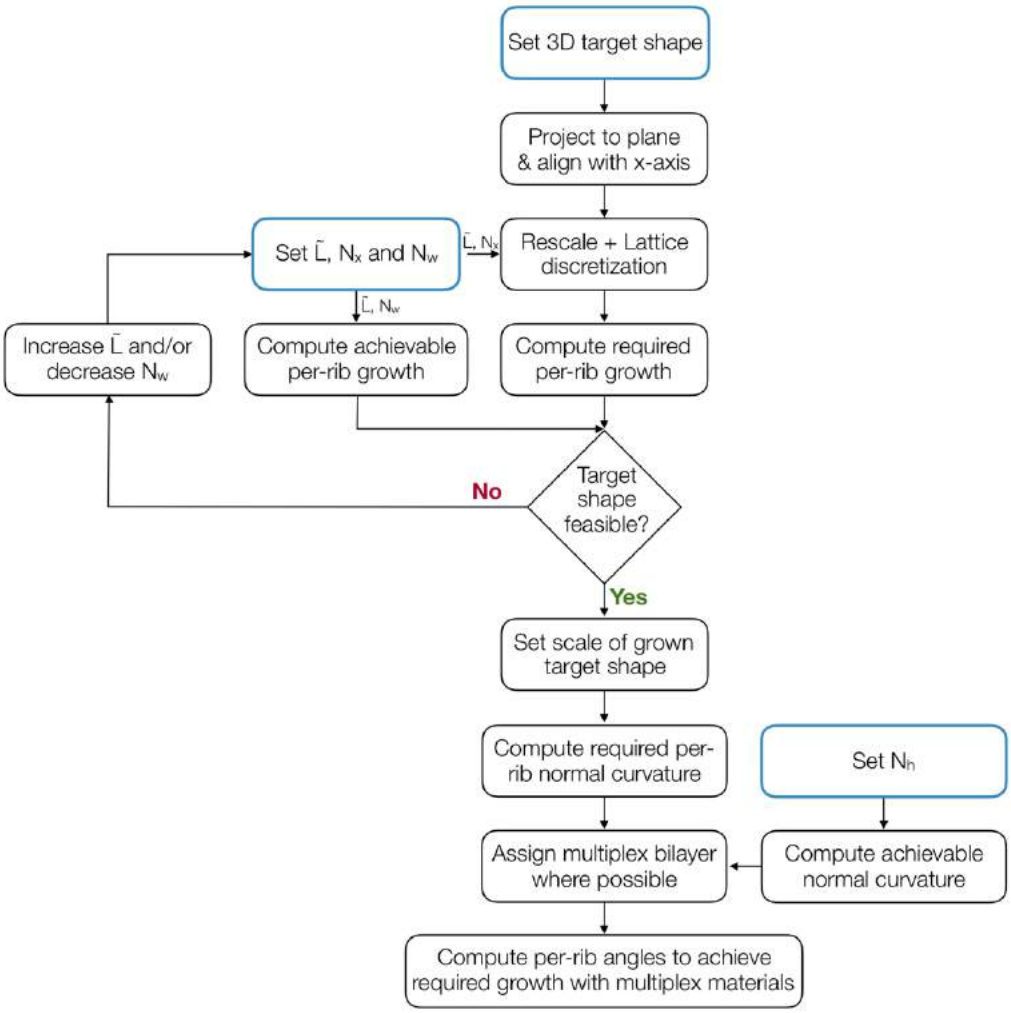

Figure S10. A flow chart showing the general workflow for designing a lattice that transforms into an arbitrary target shape. The input parameters are given inside the boxes with blue boundary: $\tilde{L}$ denotes the initial size of the lattice cells, N_x denotes the number of cells along the largest dimension of the flattened target shape, and N_w and N_h denote the number of printed filaments along the width and height of the ribs, respectively.

Table S1. Description of printed spherical caps.

Dimension $(N_x \times N_y)$	Initial Distance Between Nodes $(\bar{L})$	Number of Filaments† Along Rib Width (N_w)	Number of Filaments† Along Rib Height (N_h)	Dimensionless Sagging Deflection $(d_s/\bar{L})$	Sagging?	Critical Strain (ϵ_{crit})	Prediction Error $(1-\kappa_s/\kappa_t)$
5X5	20.0 mm	4	4	19.15	Yes	0.64×10^{-4}	N/A
10X10	6.0 mm	2	2	16.54	Yes	0.44×10^{-4}	N/A
3X3	20.0 mm	4	4	4.14	No	1.78×10^{-4}	0.08
5X5	12.9 mm	4	4	5.14	No	1.54×10^{-4}	0.24
3X3	20.0 mm	4	5	2.65	No	2.78×10^{-4}	0.28
3X3	20.0 mm	4	6	1.84	No	4.00×10^{-4}	0.31
5X5	6.0 mm	2	2	2.07	No	1.78×10^{-4}	0.34
3X3	12.9 mm	4	4	1.11	No	4.27×10^{-4}	0.34
5X5	12.9 mm	4	5	3.29	No	2.40×10^{-4}	0.37
5X5	12.9 mm	4	6	2.28	No	3.46×10^{-4}	0.56
3X3	6.0 mm	2	2	0.45	No	4.94×10^{-4}	0.72
5X5	6.0 mm	4	4	0.52	No	7.11×10^{-4}	0.84
3X3	6.0 mm	4	4	0.11	No	19.75×10^{-4}	0.86
5X5	12.9 mm	4	8	1.28	No	6.15×10^{-4}	1.00
3X3	20.0 mm	4	8	1.03	No	7.11×10^{-4}	1.00

† Filaments are approximately 0.2 mm in diameter.

Note: The dimensionless sagging deflection and critical strain are computed from the theoretical analysis explained in the main text and the methods, using the design parameters of each lattice. The prediction error is computed by comparing curvature measurements of the experimental samples with the curvature of target shapes.

Table S2. Calculated thermal response times for printed lattices.

Ambient Fluid	Type of Convection	Ambient Temperature [°C]	Heat Transfer Coefficient† $[\mathrm{W \cdot m^{-2} \cdot K^{-1}}]$	Thermal Time Response [s]
Air	Natural	-40	13.5	616.93
Air	Natural	25	13.5	1372.10
Air	Forced	-40	37.5	155.35
Air	Forced	25	37.5	464.13
Saline Water	Natural	0	525.0	0.64
Saline Water	Natural	25	525.0	0.98
Saline Water	Forced	0	10050.0	0.07
Saline Water	Forced	25	10050.0	0.16

† Values obtained from Incroprera et al.

Movie M1. Thermal cycling of a 4D printed homogeneous lattice, where $\tilde{L} = 20$ mm, $\tilde{\theta} = 171°$ and the inks used are 1:10 filled for low α and 1:10 neat for high α.

Movie M2. Printed lattice that exhibits polymorphic shapes. A heterogeneous lattice ($\tilde{L} = 12.9$ mm) composed of two inks (1:10 filled for low α and 1:10 neat for high α) morphs a spherical cap geometry due to differential contraction upon cooling ($\Delta T = -250$°C). When immersed in hexane, this lattice undergoes differential expansion via solvent swelling and morphs into a saddle geometry.

Movie M3. Shape-shifting patch antenna fabricated by multi-material 4D printing.

Movie M4. Multiplex bilayer lattice fabricated by multi-material 4D printing, which is designed to morph into the geometry of Gauss' face. Four inks are co-printed to produce this lattice, i.e., 1:10 filled (Ink 1), 1:10 neat (Ink 2), 1:30 filled (Ink 3), and 1:20 neat (Ink 4). Each ink is dyed with a different fluorophore to aid in visualization of the printing process.

Movie M5. Multiplex bilayer lattice fabricated by multi-material 4D printing that has morphed into the geometry of Gauss' face upon immersion into an aquarium containing a salt water solution (~ 240 g/L of NaCl).